

EXPLORING VARIABILITY OF TIPPERS AT COASTAL AND ISLAND
OBSERVATORIES DUE TO TEMPORAL VARIATIONS OF OCEANIC
ELECTRICAL CONDUCTIVITY

Rafael Rigaud do Amaral

Dissertation presented to the National Observatory's Graduate Program in Geophysics as a partial fulfillment of the requirements for the degree of Master in Geophysics.

Supervisor: Dra. Katia Jasbinschek dos
Reis Pinheiro

Co-Supervisor: Dr. Alexey Kuvshinov

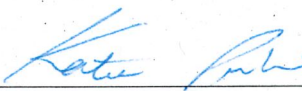
Rio de Janeiro
January of 2020

“EXPLORING VARIABILITY OF TIPPERS AT COASTAL AND ISLAND
OBSERVATORIES DUE TO TEMPORAL VARIATIONS OF OCEANIC
ELECTRICAL CONDUCTIVITY”

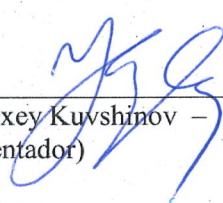
RAFAEL RIGAUD DO AMARAL

DISSERTAÇÃO SUBMETIDA AO CORPO DOCENTE DO PROGRAMA DE PÓS-
GRADUAÇÃO EM GEOFÍSICA DO OBSERVATÓRIO NACIONAL COMO PARTE
DOS REQUISITOS NECESSÁRIOS PARA A OBTENÇÃO DO GRAU DE MESTRE
EM GEOFÍSICA.

Aprovada por:



Dra. Katia Jasbinschek dos Reis Pinheiro – ON/MCTIC
(Orientadora)



Dr. Alexey Kuvshinov – ETH-Zurique
(Coorientador)



Dr. Sergio Luiz Fontes – ON/MCTIC



Dr. Naser Meqbel - GFZ

RIO DE JANEIRO – BRASIL

27 DE JANEIRO DE 2020

Rigaud do Amaral, Rafael

Exploring Variability of Tippers at Coastal and Island Observatories Due to Temporal Variations of Oceanic Electrical Conductivity/Rafael Rigaud do Amaral. – Rio de Janeiro: ON, 2020.

??, 62 p.: il.; 29,7cm.

Supervisor: Katia Jasbinschek dos Reis Pinheiro

Co-Supervisor: Alexey Kuvshinov

Dissertação (mestrado) – ON/Programa de Pós-graduação em Geofísica, 2020.

Bibliography: p. 48 – 54.

1. Geomagnetism. 2. Magnetotellurics. 3. Tippers.
I. Kuvshinov, Alexey. II. Observatório Nacional, Programa de Pós-graduação em Geofísica. III. Título.

Agradecimentos

Agradeço primeiramente à minha família. Aos meus pais, Álvaro e Edna, por sempre terem feito todo o possível para o meu bem estar e por não terem medido esforços para que eu seguisse atrás dos meus sonhos, seja agora no Rio, em Salvador, ou nos momentos difíceis de alguns anos atrás. Amo vocês. À minha irmã, agradeço o companheirismo de sempre, ao ouvido sempre disponível quando eu precisei e por seguir sempre comigo. E, claro, ao meu cunhado, Ramon, pela companheirismo de sempre.

Eu acho que tenho muita sorte de poder olhar pra trás e ver que tenho diversas amizades que se estendem há anos. Amigos que torceram por mim e compartilharam das minhas alegrias e angústias durante estes dois anos de mestrado. São eles: as Creolas (Carolzinha, Daniela Ananda, Jade, Juliana, Juliane), as caçadoras da RMS (Marina e Tati), o Mersey Shore (Derek, Isabela, Pedro), ao BRM/ as putianas (Adilson, Everaldo, Fernanda, Hellen), o Geofamily, Larissa Ottoboni, e os amigos da sala do ON (Larissa, Luis Felipe, Kris, Shay). Agradeço especialmente às minhas amigas que encararam este processo de mudança para o Rio de Janeiro comigo: Juliana, Paula e Tainã.

Agradeço aos colegas do Grupo MOSAIC, previamente conhecido como "Grupo da professora Katia Pinheiro" (Gabriel e Marcel) e aos colegas do ETH-Zürich (Chen, Daria, Elena e Federico - nos vemos em breve na Suíça!). Agradeço também ao Mikhail Kruglyakov, por ter (do jeito dele) me ajudado muito durante o desenvolvimento do meu mestrado. Poder discutir Integral Equations com ele foi um privilégio imenso. Agradeço também aos professores do Observatório Nacional, especialmente ao Daniel, Vanderlei e à Valéria pelos ensinamentos em Física da Terra Sólida, Programação e Inversão Geofísica, respectivamente.

Por fim, um agradecimento especial aos meus orientadores. Tive uma sorte enorme de poder trabalhar sob a tutela de pessoas que eu admiro ao longo destes dois anos. Ao Alexey Kuvshinov, agradeço por ter confiado este projeto complexo a mim e me dado a oportunidade e todas as ferramentas necessárias para desenvolver esta pesquisa. A trajetória não foi fácil, mas com certeza valeu a pena e fez despertar em mim o interesse pela academia. Por último, agradeço imensamente à minha orientadora, Katia Pinheiro, por ter me dado esta oportunidade e pelo cuidado que

ela tem com os seus alunos, como uma segunda mãe. Se agora eu terei a oportunidade de seguir trabalhando com o que eu amo fazer foi, em grande parte, por conta dos esforços e da visão de mundo dela. Serei sempre grato e levo ambos como exemplo na minha carreira.

Resumo da Dissertação apresentada ao Programa de Pós-Graduação em Geofísica do Observatório Nacional como parte dos requisitos necessários para a obtenção do título de Mestre em Geofísica.

EXPLORING VARIABILITY OF TIPPERS AT COASTAL AND ISLAND
OBSERVATORIES DUE TO TEMPORAL VARIATIONS OF OCEANIC
ELECTRICAL CONDUCTIVITY

Rafael Rigaud do Amaral

January/2020

O campo geomagnético registrado em observatórios magnéticos contém informações tanto de componentes indutoras (externas) quanto induzidas (internas). Este tipo de dado é tradicionalmente utilizado para investigar a condutividade elétrica do manto terrestre. Além disso, estudos recentes mostraram que tippers calculados usando medidas de curto período feitas em observatórios em ilhas são sensíveis à condutividade elétrica da litosfera oceânica e manto superior. Estes se devem a contrastes de condutividade entre rochas resistivas continentais e a água oceânica condutiva. As componentes dos tippers também apresentam variações sazonais pequenas, porém sistemáticas, que acredita-se serem devidas a mudanças nos campos magnéticos externos. Levando em consideração ambos fenômenos, neste estudo eu fiz uma modelagem numérica do efeito de condutividade elétrica oceânica em tippers estimados em observatórios localizados em ilhas. Eu modeliei a parte dos tippers que se deve a variações de condutividade oceânica em profundidade. Além disso, modeliei tippers usando variações temporais de condutividade elétrica oceânica para analisar se estas explicam parte das variações temporais observadas em estudos prévios. Eu criei modelos de condutividade tridimensionais (3-D) discretizando dados de batimetria oriundos de modelos globais. Os modelos condutivos são construídos incorporando valores realísticos de condutividade oceânica, calculados a partir de modelos globais de temperatura e salinidade. Para incorporar efeitos condutivos tridimensionais (3-D) ao longo das linhas de costas, eu modeliei os campos eletromagnéticos utilizando um código cartesiano baseado no método de equações integrais. Eu defini o efeito oceânico pela diferença entre os tippers calculados a partir de modelos com condutividade oceânica variando em profundidade e com condutividade elétrica oceânica constante (conforme feito em estudos anteriores). Eu também investiguei as variações sazonais das componentes de tippers

calculados utilizando medidas experimentais de uma distribuição global de observatórios magnéticos pertencentes ao INTERMAGNET. Os resultados da etapa de modelagem deste estudo mostram que as diferenças nos tippers devido a variações de condutividade em profundidade são observadas em parte dos observatórios magnéticos localizados em latitudes baixas e médias, regiões com elevada condutividade elétrica oceânica. A amplitude deste efeito e os períodos em que ele é observado variam dependendo da condutividade oceânica e batimetria da região de observações. Entretanto, temporalmente essas variações de condutividade têm um efeito desprezível na variabilidade temporal das componentes dos tippers. Além disso, em geral tippers calculados a partir de modelos com variações realísticas de condutividade reproduzem as observações de forma mais precisa do que aqueles calculados utilizando valores constantes de condutividade. Desta maneira, recomenda-se incorporar a condutividade elétrica dos oceanos de forma precisa ao modelar tippers em regiões oceânicas caso hajam dados disponíveis e confiáveis. A parte experimental desta dissertação foi o primeiro estudo a analisar variações sazonais de tippers em baixas latitudes e regiões equatoriais. Eu calculei tippers experimentais utilizando dados geomagnéticos utilizando um método robusto. Para incorporar efeitos sazonais, as variabilidades correspondentes foram agrupadas nas Estações Lloyd. Para a componente norte dos tippers, variações sazonais têm implicações para inversões de dados eletromagnéticos (EM) apenas em latitudes maiores do que 35° e para períodos maiores do que 1200 segundos. Além disso, nestas regiões existem grandes diferenças de amplitude entre componentes dos tippers medidas durante os solstícios de Dezembro e Junho que precisam ser levadas em consideração ao comparar tippers medidos em estações diferentes. Para a parte real da componente leste, variações sazonais podem ser relevantes para inversões de dados EM em um intervalo de latitudes maior, de -35° até 60° , e para períodos maiores do que 2400 segundos. Para a parte leste da componente imaginária, modulações sazonais são observadas em todas as latitudes em 2400 segundos, mas elas têm efeitos desprezíveis para estudos EM. Para ambas as componentes, variações de tippers medidas durante os equinócios são desprezíveis. Assim, medir tippers durante esta estação pode ser efetivo para minimizar efeitos sazonais nas regiões supracitadas. Desta maneira, os resultados de ambas as partes deste estudo evidenciam a necessidade de se considerar efeitos geomagnéticos anômalos, sejam eles oriundos dos oceanos ou de fatores externos, ao modelar e inverter tippers.

Abstract of the Dissertation presented to the National Observatory's Graduate Program in Geophysics as a partial fulfillment of the requirements for the degree of Master in Geophysics.

EXPLORING VARIABILITY OF TIPPERS AT COASTAL AND ISLAND
OBSERVATORIES DUE TO TEMPORAL VARIATIONS OF OCEANIC
ELECTRICAL CONDUCTIVITY

Rafael Rigaud do Amaral

January/2020

Geomagnetic field variations recorded at magnetic observatories contain information from both inducing (external, or source) and induced (internal) components. Such data is traditionally used to investigate electrical conductivity of the Earth's mantle. Furthermore, recent studies have shown that tippers calculated from short-period magnetic data measured at island observatories constrain electrical conductivity of the oceanic lithosphere and upper mantle. These are due to conductivity contrasts between resistive continental landmass and conductive seawater. Moreover, tippers components present small but systematic seasonal variations whose origin is believed to be associated to external magnetic source fields variations. Taking both phenomena into account, in this study I performed numerical modelling of the oceanic induction effect (OIE) on tippers estimated in island observatories. I modelled the part of tippers that is due to depth-varying oceanic conductivity. Furthermore, I modelled tippers using time-varying oceanic conductivity to analyze whether part of their temporal variability is due to temporal variations of oceanic conductivity. I created conductivity models by discretizing bathymetry data. These models incorporate realistic oceanic conductivity, which are calculated from global temperature and salinity fields. To account for three-dimensional (3-D) conductivity effects along coastlines, I modelled electromagnetic (EM) fields using a cartesian integral equation solver. I defined the OIE by the difference between tippers calculated from models incorporating depth-varying constant (with respect to depth) oceanic electrical conductivity. I also investigated the seasonal variations of experimental tipper components calculated from a global distribution of INTERMAGNET observatories. The results from the modelling part of this study show that differences in tippers due to depth-varying oceanic conductivity are observed in most of the magnetic observatories located in low to intermediate latitudes, regions where oceanic

electrical conductivity is larger than 3.2 S/m. Amplitude of this effect and period ranges where it may be observed vary depending on local oceanic conductivity and bathymetry. However, modelled temporal variations of tippers due to time-varying oceanic conductivity are negligible in comparison with observations. Nevertheless, in general tippers modelled incorporating depth-varying oceanic conductivity reproduce observations better than those calculated from constant conductivity models. Thus, it is recommended to accurately incorporate oceanic conductivity when modelling tippers in oceanic sites, if this data is available and trustworthy. The experimental part of this dissertation was the first study to analyze seasonal variations of tippers in low latitudes and equatorial regions. I calculated experimental tippers from monthly XYZ magnetic observatory data using a robust section-averaging approach. To account for seasonal effects, their corresponding variabilities were grouped into the three Lloyd Seasons of the year. For the northward tipper components, seasonal variations have implications for electromagnetic (EM) inversion only in latitudes larger than 35° and for periods larger than 1200 seconds. Moreover, in these regions there are large amplitude differences between northward tipper components measured in December and June solstices that need to be accounted for when comparing responses measured during different seasons. For the real eastward tipper component, seasonal variations can be relevant for EM inversions in a larger latitude range, from -35° to 60° , and for periods larger than 2400 seconds. For the imaginary eastward component, seasonal modulations are observed in all latitudes at 2400 seconds, but they are negligible for EM studies. For both components, variations of tippers measured during the equinox are negligible. Thus, measuring tippers during this season can be effective to minimize seasonal source effects in the aforementioned regions. Therefore, results from both parts of this dissertation highlight the necessity of taking into account anomalous geomagnetic inductive effects, either arising from the ocean or from external fields, when modelling and inverting tippers.

Contents

1	Introduction	1
2	Objetives and Motivations	4
3	Physical Fundamentals	5
3.1	EM Induction in the Earth	5
3.2	Tippers	8
3.3	3-D EM Modeling using Integral Equation Approach	11
4	Methodology	15
4.1	Estimation of Experimental Responses	15
4.2	Synthetic Data Modelling	17
4.2.1	Creation of 3-D Conductivity Model	17
4.2.2	Calculation of Global Oceanic Electrical Conductivity	20
4.2.3	3-D EM Modelling	21
5	Results	22
5.1	Modelling Study	22
5.1.1	Effects of Depth-Varying Oceanic Conductivity	22
5.1.2	Effects of Time-Varying Oceanic Electrical Conductivity	34
5.2	Experimental Data Study	37
6	Conclusions	45
	Bibliography	48
	Appendix A: Modelling of Tippers in Coastal Regions	55
	Appendix B: Abstract submitted to Earth, Planets, Space (EPS) journal	60
	Appendix C: Abstract to be submitted to Earth, Planets, Space (EPS) journal	61

List of Figures

3.1	Concept of electromagnetic (EM) induction inside the Earth by an external natural source.	6
3.2	Amplitude spectrum of the Earth's magnetic field.	7
3.3	Transformation of an input signal by a transfer function in a linear system in the frequency domain.	8
3.4	Seasonal modulations of tippers components.	10
3.5	Sketch of 3-D model used in integral equation modelling	13
4.1	Experimental tippers calculation flowchart.	15
4.2	Experimental tippers calculation flowchart.	17
4.3	1-D global conductivity model derived by GRAYVER <i>et al.</i> (2017) from the joint inversion of magnetospheric and ocean tidal magnetic signals, used as the background section in the modellings executed in this study.	18
4.4	Calculated December global oceanic electrical conductivity, depth-averaged accordingly to vertical layers with depths of 0 m to 100 m, 300 m to 400 m, 600 m to 700 m, 900 m to 1000 m, 1000 to 1500 m and 1500 to 2000 m. Green circles represent island observatories used in this study.	19
4.5	Vertical parameterization of the models used in this study. σ_{air} is the conductivity of the air, σ_1 to σ_{12} are the vertical layers where monthly depth-varying electrical conductivity are incorporated, σ_{ocean} is the deep (below 2000 m) ocean conductivity and σ_{land} is the continental landmass conductivity.	20
5.1	Magnetic observatories used in this study (green circles) and northern and southern Auroral Electrojets. Observatories information can be found in Table 5.1.	23

5.2 Ascension Island observatory (ASC) bathymetry model, regional oceanic electrical conductivity profiles, modelled and observed tippers and modelled ocean induction effects (OIE). (a) presents the top view of the bathymetry model, where the dashed line indicates the profile in (b), presenting the west-east bathymetry profile across the modelling domain. (c) presents regional depth-varying (purple) and constant with respect to depth (orange) oceanic conductivity electrical profiles, extracted from the dataset shown in Fig. 5.1. (d) to (g) present modelled (orange and red curves) and observed (blue curves) tipper components: $\Re T_x$, $\Re T_y$, $\Im T_x$, $\Im T_y$. Orange and red curves correspond respectively to tippers modelled incorporating constant and depth-varying oceanic electrical conductivity shown in Fig. 5.2 c. (h) and (i) present modelled T_x and T_y components ocean effects as red curves and the threshold of 0.025 as grey lines. 25

5.3 Same as Fig. 5.2, but for Cocos-Keeling Islands observatory (CKI) . . . 26

5.4 Same as Fig. 5.2, but for GAN observatory (GAN). 27

5.5 Same as Fig. 5.2, but for Guam observatory (GUA). 28

5.6 Same as Fig. 5.2, but for Honolulu observatory (HON). 29

5.7 Same as Fig. 5.2, but for Easter Island observatory (IPM). 30

5.8 Same as Fig. 5.2, but for Pamatai observatory (PPT). 31

5.9 Same as Fig. 5.2, but for St. Helena observatory (SHE). 32

5.10 Same as Fig. 5.2, but for Santa-Maria/Azores observatory (SMA). . . 33

5.11 Same as Fig. 5.2, but for Tristan da Cunha observatory (TDC). . . . 34

5.12 Difference between December and June oceanic electrical conductivity, depth-averaged accordingly to vertical layers with depths of 0 m to 100 m, 300 m to 400 m, 600 m to 700 m, 900 m to 1000 m, 1000 to 1500 m and 1500 to 2000 m. 35

5.13 Modelled and observed T_x component variability. 36

5.14 Modelled (dark blue circles) and observed (light blue circles) T_y component variability, for periods of 300 sec, 600 sec, 1200 sec, 2400 sec, 4800 sec and 9600 sec. The size of circles indicates four ranges of amplitudes: 0.06, 0.12, 0.18 and 0.24. 37

5.15 Magnetic observatories used in the experimental part of this study. . . 38

5.16 Global real (a) and imaginary (b) T_x component variabilities for periods of 300 s, 600 s, 1200 s, 2400 s, 4800 s and 9600 s. The blue, red and yellow circles represent D, J and E seasonal variabilities, respectively. Gray and blue dashed lines correspond to the geographic equator and $\pm 40^\circ$ latitudes, respectively. Green dashed lines represent the threshold defining the minimum tipper amplitudes with implications to EM inversion (± 0.025). The error bars are calculated for each period and season from the corresponding monthly tippers errors. 41

5.17 Difference between D and J real (a) and imaginary (b) T_x seasonal variabilities (purple circles) for periods of 300 s, 600 s, 1200 s, 2400 s, 4800 s and 9600 s. Gray and blue dashed lines correspond to the geographic equator and $\pm 40^\circ$ latitudes, respectively. Green dashed lines represent the threshold defining the minimum tipper amplitudes with implications to EM inversion (± 0.025). The error bars are calculated for each period and season from the monthly tippers errors. 42

5.18 Same as Fig. 4.4, but for real (a) and imaginary (b) T_y seasonal variabilities. 43

5.19 Same as Fig. 5.17, but for real (a) and imaginary (b) T_y seasonal variabilities. 44

A1 Global sediments thickness map. 56

A2 Tatuoca observatory conductivity model and map. 57

A3 King Edward Point observatory bathymetry model, oceanic conductivity profiles, modelled and observed tippers and modelled ocean effect. 58

A4 Port Stanley observatory bathymetry model, oceanic conductivity profiles, modelled and observed tippers and modelled ocean effect. . . 59

Chapter 1

Introduction

Geophysical methods based on electromagnetic (EM) induction are one of the main techniques used to investigate the electrical conductivity of the Earth's crust and mantle (CHAVE and JONES, 2012; YOSHINO, 2010). On this regard, geomagnetic field variations recorded at magnetic observatories contain information from both inducing (external, or source) and induced (internal) components. Traditionally, times series of hourly-mean of geomagnetic data, with periods longer than one day, are used to investigate mantle conductivity variations. For this period range, observed geomagnetic field variations are originated in the magnetospheric ring current. The technique of determining the Earth's mantle conductivity from such data is commonly referred to as "Geomagnetic Depth Sounding" (BANKS, 1969; ?). However, the uneven distribution of magnetic observatories at the Earth's surface restricts the application of this technique to the determination of one-dimensional (1-D) conductivity profiles, beneath a considered observatory. Nevertheless, this methodology has been successfully employed in multiple studies, on regional and global scales (e.g. KUVSHINOV *et al.*, 2005; MUNCH *et al.*, 2018; OLSEN, 1998; SHIMIZU *et al.*, 2010; UTADA *et al.*, 2003).

Recent developments in geomagnetic observatory instrumentation enabled the measurement of magnetic field data at up to 1 Hz sampling rate. Thus, short-period electromagnetic responses could be estimated using data ranging from a few seconds to hours. Considering the aforementioned period range, it is possible to approximate external magnetic source fields as vertically incident plane-waves in mid-latitude observatories and calculate vertical magnetic transfer functions, more commonly referred to as tippers, from magnetic observatory data. These are associated to the "tip" of the vertical geomagnetic field component due to lateral conductivity anomalies. Therefore, tippers are zero for purely 1-D conductivity variations (BERDICHEVSKY and DMITRIEV, 2008). However, at island and coastal observatories, the Ocean Induction Effect (OIE) (PARKINSON and JONES, 1979), which is due to lateral conductivity contrasts between resistive continental landmass and

conductive oceanic seawater, alliviates this limitation and thus large tippers can be measured even if the underlying conductivity distribution beneath the observatory is 1-D (SAMROCK and KUVSHINOV, 2013). Furthermore, MORSCHHAUSER *et al.* (2019) have shown that, in island observatories, tippers constrain the electrical conductivity of oceanic lithosphere and upper mantle. This is a promising technique to execute EM soundings in remote oceanic regions. However, it relies on an accurate incorporation of three-dimensional (3-D) effects, arising from bathymetry, into modelling.

Inaccuracy in tippers measurements may also arise from any deviations of the ideal plane-wave mode of propagation (e.g. GRAYVER *et al.*, 2019; HERMANCÉ, 1978; MURPHY and EGBERT, 2018). Those are known as source effects and, in this situation, responses contain information from the anomalous source fields, and not only from the underlying conductivity distributions. Interpretation of source-field affected tippers may lead to severely biased results (e.g. MARESCHAL, 1986; SOKOLOVA and VARENTSOV, 2007; VILJANEN *et al.*, 1999).

Source effect in tippers cause small but systematic temporal variations which are believed to be due to changes in magnetic source fields. These variations increase with increasing latitude and period of measurements (BEAMISH, 1979; TAKEDA, 1997). Particularly, ARAYA VARGAS and RITTER (2016) identified periodic seasonal variations in mid-latitude observatories, characterized by a high and low peaks of the real northward component during the December and June solstice, respectively. The same pattern was observed in the imaginary part, but with opposite polarization. On the other hand, while seasonal variations are also observed on the eastward component, these do not follow a clear geographical pattern as their northward counterpart and could not be explained by a empirical model. This raises a question if other factors could influence temporal variations of tipper components.

Taking all these factors into account, the aim of this study is to determine the part of tippers measured in island observatories that is due to oceanic electrical conductivity variations in depth. I also investigate whether part of tipper components seasonal variations is explained by temporal variations of oceanic electrical conductivity. For this purpose, I performed numerical modelling of these effects. Realistic global oceanic electrical conductivity was calculated from temperature, salinity and pressure. Ocean conductivity is rigorously incorporated into conductivity models constructed by discretization of bathymetry data. I model EM fields using a cartesian 3-D integral equation solver. Effects of tippers due to depth and time varying oceanic conductivity are analyzed in order to identify the regions and period ranges where they have implications of EM inversions.

I also investigated seasonal variations of tipper components on a global scale using a worldwide distribution of INTERMAGNET observatories. To account for sea-

sonal variations, I calculated tippers using monthly geomagnetic data and grouped them into the Lloyd seasons of the year. I defined the latitude and period ranges where these variations can be relevant for EM inversions. Therefore, both parts of this study (modelling and experimental) will complement each other, providing a comprehensive analysis of the anomalous effects on tippers, arising from the ocean and external sources.

Chapter 2

Objetives and Motivations

The main objective of this thesis is to investigate the effects of oceanic electrical conductivity, varying in depth and time, on tippers that are calculated in island observatories. In coastlines, the amplitude of tippers depend on the conductivity contrast between the continental landmass and oceanic seawater and on the distance from the ocean. Since tippers are widely used on the interpretation and inversion of magnetotelluric (MT) data, it is fundamental to study and quantify oceanic effects on tippers in order to provide a correct interpretation of MT results. This is the first study to rigorously incorporate realistic oceanic conductivity effects into EM modelling of tippers. Thus, its results will provide an initial guideline on the locations, amplitude and period ranges where the oceanic effect needs to be accounted for.

Other anomalous effects on tippers, arising from magnetic source fields, will be analyzed on the experimental study of seasonal modulations on tippers measured on a global distribution of magnetic observatories. Previous studies did not include observatories near the equator because it was considered that the Equatorial Electrojet (YAMAZAKI and MAUTE, 2017) introduced errors on measurements. However, it was shown that this feature has a negligible inductive effect (e.g. KUVSHINOV *et al.*, 2007) on both tippers and magnetotelluric impedances (SAMROCK *et al.*, 2015). Therefore, the use of a measurements on a global scale is a novel and important contribution of this study, specially to improve studies in low latitude regions.

Chapter 3

Physical Fundamentals

3.1 EM Induction in the Earth

In EM induction studies, electric and magnetic fields of natural origin are used to investigate electrical conductivity distributions in the subsurface. This phenomena is based on the inter-generation of the aforementioned fields. A primary time-varying electrical current, associated to an external electric source field, induces a time-varying magnetic field. The latter induces an electric current in the subsurface, which induces a secondary magnetic field that can be measured in the surface of the Earth (Fig. 3.1). Inducing and induced fields are commonly referred to in geophysical literature as primary and secondary fields, respectively (NABIGHIAN, 1991b). Therefore, measurements taken above the Earth's surface contain contributions from both components.

Mathematically, the propagation of electric and magnetic fields are described by Maxwell's Equations. In the frequency domain, those are defined as

$$\nabla \times \mathbf{H}(\mathbf{r}, \omega) = \sigma \mathbf{E}(\mathbf{r}, \omega) + \mathbf{j}^{ext}(\mathbf{r}, \omega) \quad (3.1)$$

$$\nabla \times \mathbf{E}(\mathbf{r}, \omega) = -i\omega\mu\mathbf{H}(\mathbf{r}, \omega), \quad (3.2)$$

where $\mathbf{E}(\mathbf{r}, \omega)$, $\mathbf{H}(\mathbf{r}, \omega)$ and $\mathbf{j}^{ext}(\mathbf{r}, \omega)$ are the position and frequency dependent electric and magnetic fields and external current density, respectively; \mathbf{r} is the position vector, in cartesian coordinates; ω is the angular frequency, defined as $\omega = 2\pi/p$, where p is the period of the signal; μ is the magnet permeability which is assumed to be constant and equal to the magnetic permeability in the free space, $\mu_0 = 4\pi 10^{-7}$ N/A² and σ is the conductivity distribution in the Earth. It is assumed that displacement currents are negligible in the period range of natural sources. The magnetic

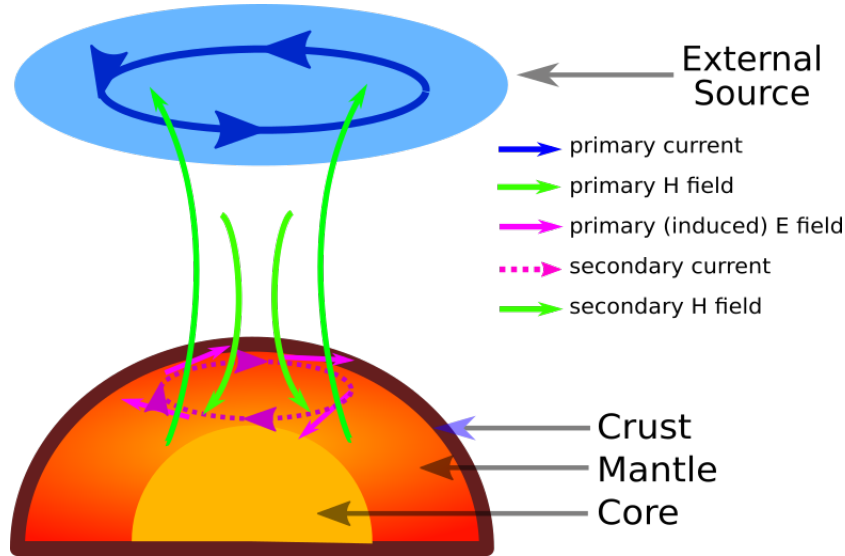


Figure 3.1: Concept of EM induction inside the Earth by an external natural source. A primary time-varying external electric current induces a magnetic field that propagates inside the Earth. It induces an electric current that, consequently, induces a secondary magnetic field that can be measured at the Surface.

field is related to the magnetic flux density field via $\mathbf{H}(\mathbf{r}, \omega) = \mathbf{B}(\mathbf{r}, \omega)/\mu$. Following the convention traditionally adopted in geophysical literature, hereinafter \mathbf{B} will be referred to as magnetic field (NABIGHIAN, 1991a).

For EM studies to be feasible, it is necessary to assume that the time-varying external source fields are observed as vertically plane incident waves at the surface of the Earth (plane wave assumption) (SIMPSON and BAHR, 2005). Mathematically, for the applicability of this condition to be guaranteed, the spatial wavelength of the source (λ) must be much larger than the depth of penetration of the induced currents (δ), i.e., $\lambda \gg \delta$, where the EM skin depth (in km) is given by

$$\lambda \gg \delta = \frac{\sqrt{\rho T}}{2}, \quad (3.3)$$

and ρ is the resistivity of the medium where the EM wave is propagating, defined as the inverse of conductivity. From the skin depth concept, it is clear that longer period signals are associated to deeper soundings of the Earth.

The plane wave assumption is valid for EM field source of simple geometry, corresponding to period ranges from 0.1 seconds to 3 hours (Fig. 3.2). For longer periods, external geomagnetic fields are originated by complex sources, such as the Solar Quiet (Sq) current system and the magnetospheric ring current (KUVSHINOV, 2012). In this case, the plane-wave assumption is no longer valid and more complex mathematical schemes are required to represent these sources (cf. GUZAVINA *et al.*, 2019; PÜTHE *et al.*, 2015). Regions under the influence of Auroral

Electrojets are also associated with violations of the plane wave assumption, in all period ranges (e.g. JONES and SPRATT, 2002).

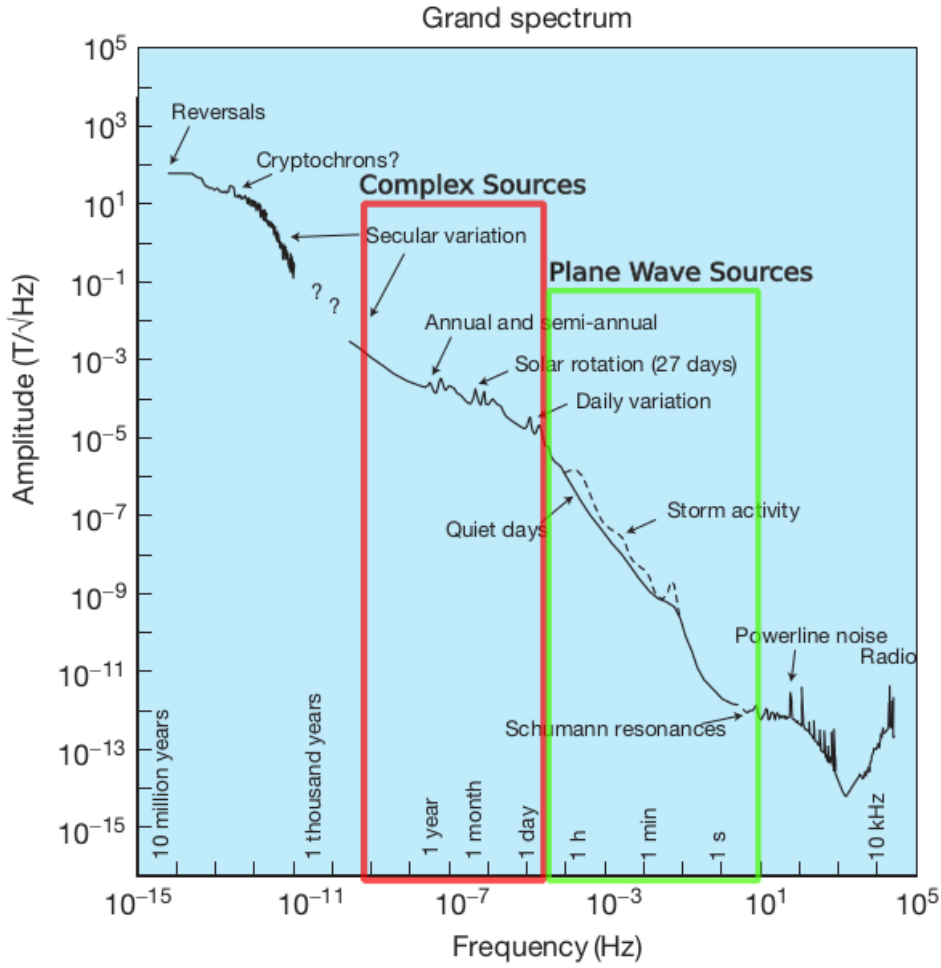


Figure 3.2: Amplitude spectrum of the Earth's magnetic field. Red and green circles highlight periods associated with complex and plane wave sources, respectively. Modified from CONSTABLE (2015).

The inter-relations between propagating EM fields and the conducting Earth are described by transfer functions. Those are mathematical representations of the relations between input and output signals of a linear system in the frequency domain (GIROD *et al.*, 2001). Given the linearity of the Maxwell's Equations, it is possible to consider the Earth as a linear system and apply this concept to EM sounding (PÜTHE *et al.*, 2015). Through the use of these functions, it is possible to determine the response of a system to a specified source. For a given input signal in the frequency-domain $\mathbf{X}(\omega)$ that is transformed by a transfer function $\mathbf{M}(\omega)$ into an output signal $\mathbf{Y}(\omega)$ (Fig. 3.3), the following relation holds

$$\mathbf{Y}(\omega) = \mathbf{X}(\omega)\mathbf{M}(\omega) \quad (3.4)$$

and, if input and outputs signals are known, the associated transfer function can be determined. The correlation between these signals is defined as coherency and it measures the proportion of the output signal that can be explained by the considered input. Details of the statistical approach used in its calculation can be found in PÜTHE (2015).

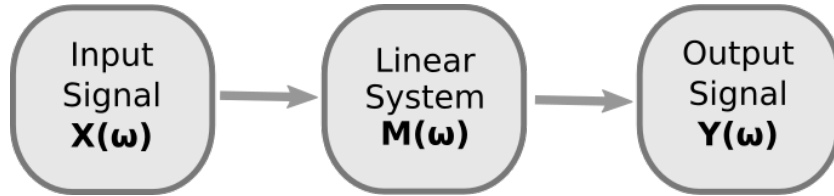


Figure 3.3: Illustration of a linear system in the frequency domain, where the input signal $\mathbf{X}(\omega)$ is transformed into an output signal $\mathbf{Y}(\omega)$ by a transfer function $\mathbf{M}(\omega)$.

Considering EM studies, transfer functions can be determined by primary and secondary field electric and/or magnetic field components. Then, electrical conductivity of the Earth's interior can be determined by the inversion of these functions (ASTER *et al.*, 2005). The most widely used transfer function in geophysical induction studies is the magnetotelluric (MT) impedance, that is defined as a second-order tensor relating horizontal components of electric and magnetic fields,

$$\mathbf{E}(\mathbf{r}, \omega) = \mathbf{Z}(\mathbf{r}, \omega)\mathbf{H}(\mathbf{r}, \omega) \quad (3.5)$$

where $\mathbf{Z}(\mathbf{r}, \omega)$ is the position and frequency dependent MT impedance tensor. The previous equation can be expanded as

$$\begin{pmatrix} E_x(\mathbf{r}, \omega) \\ E_y(\mathbf{r}, \omega) \end{pmatrix} = \begin{pmatrix} Z_{xx}(\mathbf{r}, \omega) & Z_{xy}(\mathbf{r}, \omega) \\ Z_{yx}(\mathbf{r}, \omega) & Z_{yy}(\mathbf{r}, \omega) \end{pmatrix} \begin{pmatrix} H_x(\mathbf{r}, \omega) \\ H_y(\mathbf{r}, \omega) \end{pmatrix}, \quad (3.6)$$

and E_i and H_i , ($i \in [x, y]$) are the electric and magnetic fields components measured in the northward and eastward directions, respectively. In MT studies, electrical conductivity of the Earth can be determined from the surface to approximately 350 km depth (CONSTABLE, 2015).

3.2 Tippers

Another transfer function that can be determined from geomagnetic field measurements is the vertical magnetic transfer function, more commonly referred as tipper. It is defined as a measure of the tipping of the vertical magnetic field component out

of the horizontal plane in the presence of lateral conductivity anomalies (PARKINSON, 1959). Therefore, tippers are zero if conductivity varies in one direction only (BERDICHEVSKY and DMITRIEV, 2008). Assuming plane wave excitation, they relate the horizontal and vertical components of the geomagnetic field in the frequency domain by

$$B_z(\mathbf{r}, \omega) = T_x(\mathbf{r}, \omega)B_x(\mathbf{r}, \omega) + T_y(\mathbf{r}, \omega)B_y(\mathbf{r}, \omega), \quad (3.7)$$

where T_x and T_y are the complex and dimensionless components of the tipper vector \mathbf{T} , \mathbf{r} is the position vector in cartesian coordinates and B_x , B_y and B_z are the northward, eastward and vertical geomagnetic field components, respectively, and z is the vertical axis coordinate, considered positive towards the Earth's interior.

Real and imaginary components of tippers are usually plotted as induction arrows, which are expressed by $-(\Re T_x, \Re T_y)$ and $-(\Im T_x, \Im T_y)$ and point towards conductivity anomalies, assuming the Parkinson convention is used (PARKINSON, 1959). The imaginary component also gives the direction of the derivative of the real component with respect to the y axis (MARCUELLO *et al.*, 2005). Thus, the real part of tippers reach maximum amplitude at the period where the maximum conductivity contrast within the penetrated volume is observed. Moreover, at this period the imaginary part revert its polarization (DOSSO and CHEN, 2000). Therefore, analysis of tippers components gives a qualitative interpretation of conductivity variations with varying depths (GREGORI and LANZEROTTI, 1980).

In magnetic observatories in the vicinity of the ocean, large tippers can be calculated even if the underlying conductivity structure is 1-D. This is due to lateral conductivity contrasts between the conductive sea water and resistive continental rocks. This phenomenon is commonly referred as the geomagnetic coast effect and is characterized by an anomalous B_z/B_y ratio along coastlines (PARKINSON and JONES, 1979; SAMROCK and KUVSHINOV, 2013). In this situation, and assuming the use of the Parkinson convention, induction arrows point towards the nearest ocean and are perpendicular to the coastline.

Over the time, tippers present periodic variations that are believed to be modulated by the time-varying magnetic source fields (e.g BEAMISH, 1979, 1980; BRÄNDLEIN *et al.*, 2012; TAKEDA, 1997). Source effects on tippers are observed in period ranges and/or locations where the plane-wave assumption is violated (cf. Eq. 3.3). Variations in wavelength of source magnetic fields and complex sources such as the Auroral Electrojets also cause source effects (e.g HERMANCE, 1978; JONES and SPRATT, 2002; MURPHY and EGBERT, 2018). The use of source affected responses may lead to severely biased interpretations because they contain information from the

anomalous source field, and not only from the underlying conductivity distributions (SOKOLOVA and VARENTSOV, 2007; VILJANEN *et al.*, 1999).

Furthermore, ARAYA VARGAS and RITTER (2016) identified systematic periodic variations correlated to external magnetic field changes in mid-latitude observatories. The most ubiquitous patterns are a long term trend correlated to the 11-yr solar cycle and periodic seasonal modulations of the T_x components. These modulations are characterized by a high and positive peak of the $\Re T_x$ component around the June solstice and a low peak around the December solstice. The $\Im T_x$ component presents the same pattern but with opposite seasonal polarization (Fig. 3.4). These effects increase with increasing latitude and period. Seasonal modulations were also observed in the $\Re T_y$ component, but they do not follow a clear geographical pattern as in T_x .

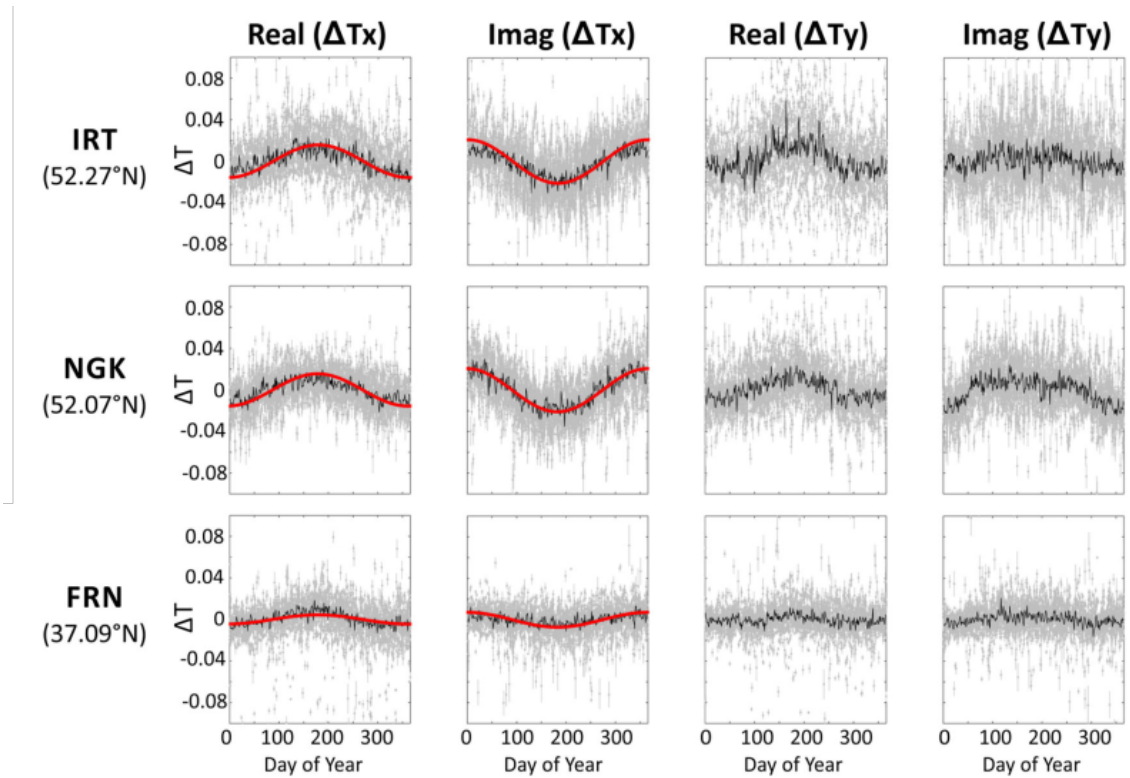


Figure 3.4: Seasonal modulations of tippers components observed in Irkutsk (IRT), Niemegek (NGK) and Fresno (FRN) observatories. Black points are daily variabilities, red points are a polynomial fit of this data and gray points are their uncertainties. Modified from ARAYA VARGAS and RITTER (2016).

3.3 3-D EM Modeling using Integral Equation Approach

3-D EM simulations are a core part of any EM induction study, being used as an engine for 3-D EM inversion, to test hypothetical 3-D conductivity models and as a tool to support feasibility studies (AVDEEV, 2005). The goal of EM modeling is to compute electric and magnetic fields over a given region by numerically solving Maxwell's equations (Eq. 3.1 and 3.2) over a discretized model that represents the region of interest.

Three different techniques are used for this purpose: finite-difference (FD), finite-element (FE) and integral equation (IE) methods. For decades, FD techniques (e.g. EGBERT and KELBERT, 2012) were the most used by the EM community. However, recently, FE (e.g. FARQUHARSON and MIENSOPUST, 2011; GRAYVER and KOLEV, 2015) and IE (e.g. KRUGLYAKOV *et al.*, 2016; SEMENOV and KUVSHINOV, 2012) methods grew in popularity. Since then, recent developments of IE concepts made modern IE solvers competitive with the most advanced FE-based codes.

IE solvers have several advantages over other approaches, as summarized in PANKRATOV and KUVSHINOV (2015). They are, in general, less demanding than FD and FE solvers, in terms of cell size, because numerical differentiation is not involved in calculation. Another advantage is that IE-based solvers work with compact system matrices and the modeling region is restricted to 3-D anomalies. On the other hand, FD and FE solvers require the discretization of a much larger volume in order to stabilize fields at the boundaries of the model.

In summary, the basic principle of IE codes is that modelled EM fields are due to a 3-D conductivity anomaly embedded in a background one-dimensional (1-D) conductivity distribution. The 1-D part of the model can be calculated analytically, while the 3-D anomaly has to be calculated using numerical methods. EM fields are calculated using Green's Tensors, which corresponds to the response of a system to an impulse function (BESIERIS and COMPTON, 1967). Those are then used to model fields on the entirety of the modelling domain via convolution volume integrals. As long as the background model remains unchanged, Green's tensors only need to be calculated once. Therefore, IE solvers are more efficient when repeated forward modellings are required.

A particular class of IE solvers, named as Contracting Integral Equation (CIE), have a remarkable advantage: after discretization, the system of linear equations is well-conditioned independent of frequency, discretization or conductivity variations (PANKRATOV and KUVSHINOV, 2015). The fundamentals of the CIE approach are presented as follows:

Considering a 3-D conductivity distribution σ in a determined model (Fig. 3.5) and taking into account the following assumptions:

- The conductivity distribution can be represented by a 3-D conductivity anomaly $\sigma_a(\mathbf{r})$, embedded in a 1-D background conductivity $\sigma_b(z)$;
- All materials are non-magnetic;
- The magnetic permeability is μ_0 in this region;
- Low frequencies are considered, thus displacement currents can be neglected (quasi-static approximation, e.g. NABIGHIAN, 1991a);
- The model is excited by an electric current density \mathbf{j}^{imp} .

The electric field, \mathbf{E} (for simplicity, hereinafter the dependence on ω and \mathbf{r} for all quantities besides conductivities will be omitted), and magnetic field, \mathbf{H} , excited by this source obey Maxwell's equations:

$$\begin{cases} \nabla \times \mathbf{H} = \sigma \mathbf{E} + \mathbf{j}^{imp} \\ \nabla \times \mathbf{E} = i\omega\mu_0 \mathbf{H}. \end{cases} \quad (3.8)$$

To solve Equation 3.8, first it is needed to find a solution of Maxwell's equations in the background conductivity model

$$\begin{cases} \nabla \times \mathbf{H}_b = \sigma_b \mathbf{E}_b + \mathbf{j}^{imp} \\ \nabla \times \mathbf{E}_b = i\omega\mu_0 \mathbf{H}_b \end{cases} \quad (3.9)$$

where \mathbf{E}_b and \mathbf{H}_b are background electric and magnetic fields, respectively. If fundamental solutions ("current-to-electric", $G_{\sigma_b}^{ej}$, and "current-to-magnetic", $G_{\sigma_b}^{hj}$ tensor Green's functions) can be calculated, \mathbf{E}_b and \mathbf{H}_b can be determined through convolution integrals

$$\mathbf{E}_b(\mathbf{r}) = \int_{\mathbb{V}_{ext}} G_{\sigma_b}^{ej}(\mathbf{r}, \mathbf{r}') \mathbf{j}^{imp}(\mathbf{r}') dv' \quad (3.10)$$

$$\mathbf{H}_b(\mathbf{r}) = \int_{\mathbb{V}_{ext}} G_{\sigma_b}^{hj}(\mathbf{r}, \mathbf{r}') \mathbf{j}^{imp}(\mathbf{r}') dv', \quad (3.11)$$

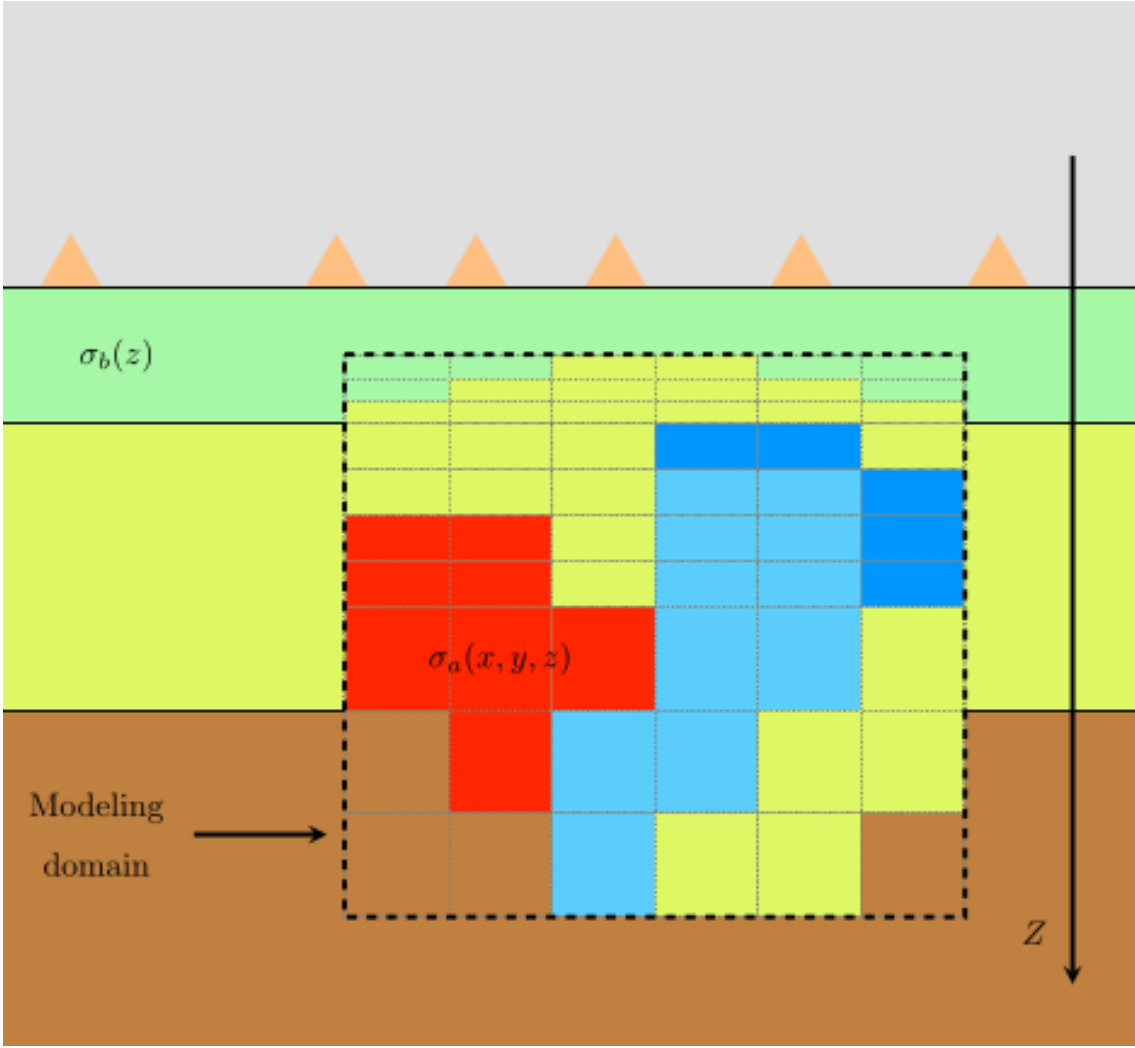


Figure 3.5: Sketch of a generic 3-D conductivity model used in integral equation modelling. Triangles represent observation sites. Extracted from KRUGLYAKOV *et al.* (2016).

where \mathbb{V}^{ext} is the volume occupied by the external current density \mathbf{j}^{imp} , $\mathbf{r} \in \mathbb{R}^3$ and $\mathbf{r}' \in \mathbb{V}^{ext}$. Note that Green's tensors depend only on \mathbf{r} , \mathbf{r}' , ω and on the 1-D conductivity distribution $\sigma_b(z)$.

Considering a modelling region \mathbb{V}^{mod} occupied by anomalies and where $\sigma_a = \sigma(\mathbf{r}) - \sigma_b(z)$ and introducing "scattered fields" $\mathbf{E}_s = \mathbf{E} - \mathbf{E}_b$ and $\mathbf{H}_s = \mathbf{H} - \mathbf{H}_b$ which, following the analytical development described in KRUGLYAKOV *et al.* (2016), can be determined via

$$\mathbf{E}_s(\mathbf{r}) - \int_{\mathbb{V}^{mod}} G_{\sigma_b}^{ej}(\mathbf{r}, \mathbf{r}') [\sigma(\mathbf{r}') - \sigma_b(z')] \mathbf{E}_s(\mathbf{r}') dv' = \mathbf{E}_0(\mathbf{r}) \quad (3.12)$$

with

$$\mathbf{E}_0(\mathbf{r}) = \int_{V^{mod}} G_{\sigma_b}^{ej}(\mathbf{r}, \mathbf{r}') \mathbf{j}^s(\mathbf{r}') dv' \quad (3.13)$$

and $\mathbf{j}^s = (\sigma - \sigma_b)\mathbf{E}_b$, $\mathbf{r} \in \mathbb{R}^3$, $\mathbf{r}' \in \mathbb{V}^3$. After discretization, Eq. 3.12 can be solved using Krylov subspace iterations (GREENBAUM, 1997). In order to stabilize the solution, particularly for highly contrasting models, the aforementioned equation is modified to an integral equation with contracting operator by

$$\chi(\mathbf{r}) - \int_{V^{mod}} K(\mathbf{r}, \mathbf{r}') R(\mathbf{r}') \chi(\mathbf{r}') dv' = \chi_0(\mathbf{r}), \quad (3.14)$$

where

$$R = \frac{\sigma - \sigma_b}{\sigma + \sigma_b}, \quad (3.15)$$

$$K(\mathbf{r}, \mathbf{r}') = \delta(\mathbf{r}, \mathbf{r}') I + 2\sqrt{\sigma_b(z)} G_{\sigma_b}^{ej}(\mathbf{r}, \mathbf{r}') \sqrt{\sigma_b(z')}, \quad (3.16)$$

$$\chi_0(\mathbf{r}) = \int_{V^{mod}} K(\mathbf{r}, \mathbf{r}') \frac{\sqrt{\sigma_b(z')}}{\sigma(\mathbf{r}') + \sigma_b(z')} \mathbf{j}^s(\mathbf{r}') dv', \quad (3.17)$$

$$\chi = \frac{1}{2\sqrt{\sigma_b}} \{(\sigma + \sigma_b)\mathbf{E}_s + \mathbf{j}^s\}, \quad (3.18)$$

$\delta(\mathbf{r}, \mathbf{r}')$ is Dirac's delta function and I is the identity operator.

Briefly, the cartesian CIE approach works according to the following steps:

1. Discretization of the modelling domain into $N_x \times N_y \times N_z$ rectangular prisms;
2. Solve the linear system $\mathbf{A}\mathbf{x} = \mathbf{b}$, where $\mathbf{x} = \chi$, $\mathbf{b} = \chi_0$ and $\mathbf{A} = (I - KR)$;
3. Calculation of elements of \mathbf{A} via integrals of corresponding elements of Green's operator $G_{\sigma_b}^{ej}$

More details on the mathematical developments presented on this section are beyond the scope of this dissertation and the reader is referred to PANKRATOV *et al.* (1995) and KRUGLYAKOV *et al.* (2016).

Chapter 4

Methodology

This thesis is the result of an ongoing collaboration between Observatório Nacional (ON), ETH-Zürich and German Research Centre for Geosciences (GFZ-Potsdam). Therefore, different scientists made contributions to the development of the codes used in this dissertation. The following subsections explain how the experimental data and modelling parts of this study were developed. All the codes developed by the author of this dissertation were written in Python language.

4.1 Estimation of Experimental Responses

The code used for calculating tippers from magnetic observatory data was developed by PÜTHE (2015) in MATLAB language. The code has an universal character, since it can be used to calculate any transfer function of interest. For this study, it was used to calculate tippers from magnetic observatory data, accordingly to the following methodology (Fig. 4.1):

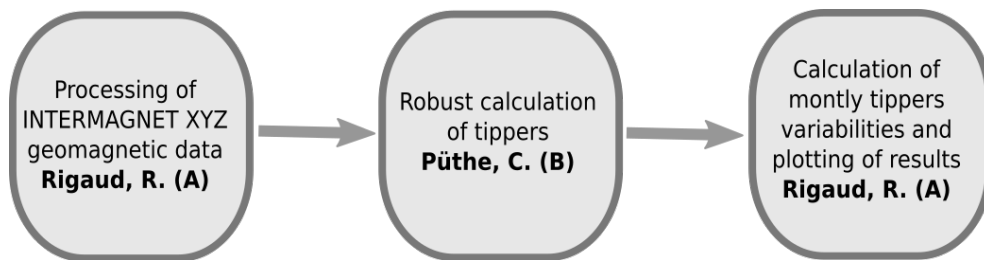


Figure 4.1: Flowchart describing the steps to calculate experimental tippers. Developers of the corresponding codes are depicted in bold. (A) ON; (B) ETH-Zürich.

1. Download of data from INTERMAGNET database. 30 days of geomagnetic data (X , Y and Z components) are used to calculate tippers (SAMROCK and KUVSHINOV, 2013);

2. Removal of outliers from data, if necessary. Data with significant gaps (larger than 5 days) were excluded from this study;
3. Separate measurements of horizontal and vertical components of the geomagnetic field into matrix and vector format, respectively (see Eq. 3.7). For example, considering a time series consisting of n measurements of B_x , B_y and B_z from a given observatory, vertical components are stored into a vector $[B_{z1}, B_{z2}, \dots, B_{zn}]^T$ and horizontal components are stored in a matrix

$$\mathbf{B} = \begin{bmatrix} B_{x1} & B_{y1} \\ B_{x2} & B_{y2} \\ \vdots & \vdots \\ B_{xn} & B_{yn} \end{bmatrix} \quad (4.1)$$

forming the following linear system

$$\begin{bmatrix} B_{x1} & B_{y1} \\ B_{x2} & B_{y2} \\ \vdots & \vdots \\ B_{xn} & B_{yn} \end{bmatrix} \begin{bmatrix} T_x \\ T_y \end{bmatrix} = \begin{bmatrix} B_{z1} \\ B_{z2} \\ \vdots \\ B_{zn} \end{bmatrix}; \quad (4.2)$$

4. Fourier transformation of segments of the time series (OLSEN, 1998), which are tapered to decrease spectral leakage. Tippers were calculated in 19 periods between 120 s and 3 hours, with a sampling interval of 60 s;
5. Solve Eq. 4.2 by using the iteratively re-weighted least squares estimator with Huber norm (e.g. ASTER *et al.*, 2005; HUBER, 1981). The code outputs real and imaginary part of tippers, their errors and coherencies. More details on the mathematical calculation of statistical parameters can be found on SEMENOV (2011) and PÜTHE (2015).
6. Calculate monthly tippers and variabilities. Experimental variability of a determined tipper component ($\Delta(T_{i,j,m})$) is defined as

$$\Delta(T_{i,j,m}) = T_{i,j,m} - \widehat{T}_{i,j} \quad (4.3)$$

where $T_{i,j,m}$ is the corresponding tipper component ($i, j \in [x, y]$) calculated

using data from the m -th month and $\widehat{T}_{i,j}$ is the median of tippers calculated in the year.

4.2 Synthetic Data Modelling

The goal of synthetic data modelling is to model EM fields and tippers using a 3-D cartesian model that reproduces the island observatory of interest. This modelling is performed in three different steps: (i) construction of a 3-D conductivity model by discretization of bathymetry data; (ii) modelling of EM fields using the IE solver PGIEM2G, described in KRUGLYAKOV and KUVSHINOV (2018); and (iii) calculation of tippers using depth and time varying oceanic conductivity models. The modelling steps are described in the following subsections and in Fig. 4.2.

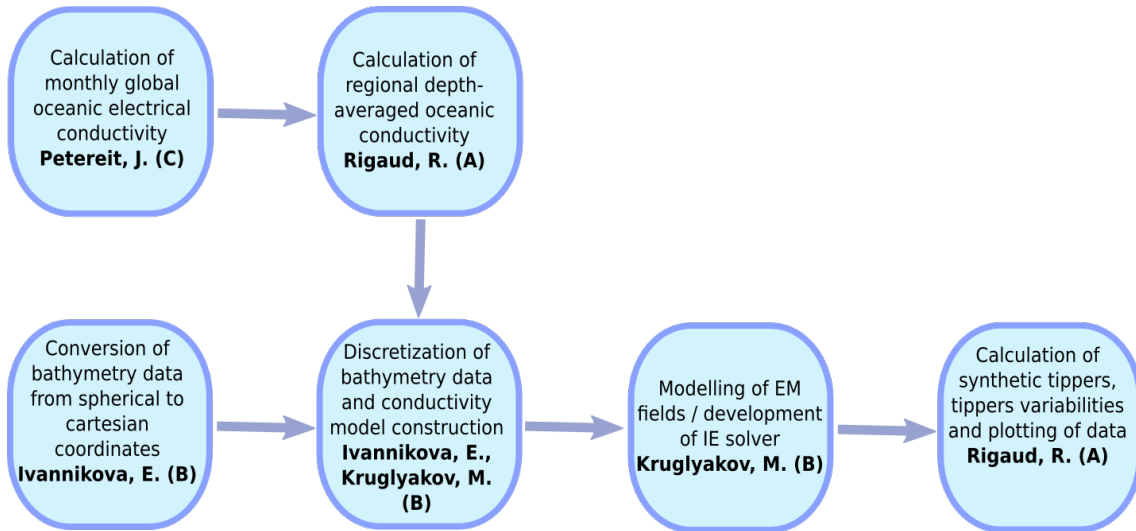


Figure 4.2: Flowchart describing the steps to calculate modelled tippers. Developers of the corresponding codes are depicted in bold. (A) ON; (B) ETH-Zürich; (C) GFZ-Potsdam.

4.2.1 Creation of 3-D Conductivity Model

The conductivity models we construct are composed by a 3-D anomaly, which approximates the nonuniform oceans surrounding the island observatories, embedded in a 1-D background conductivity section (see Fig. 3.5). As the background section, we use the 1-D global conductivity profile derived by GRAYVER *et al.* (2017) from the joint inversion of magnetospheric and ocean tidal magnetic signals extracted from Swarm and CHAMP data (Fig. 4.3). From the surface until the maximum depth of the 3-D anomaly, background conductivity is set as the ocean conductivity.

The 3-D part of our models is constructed using available bathymetry data from the National Oceanic and Atmospheric Administration (NOAA) ETOPO1 Global Relief Model (AMANTE and EAKINS, 2009). This data set is provided in spherical

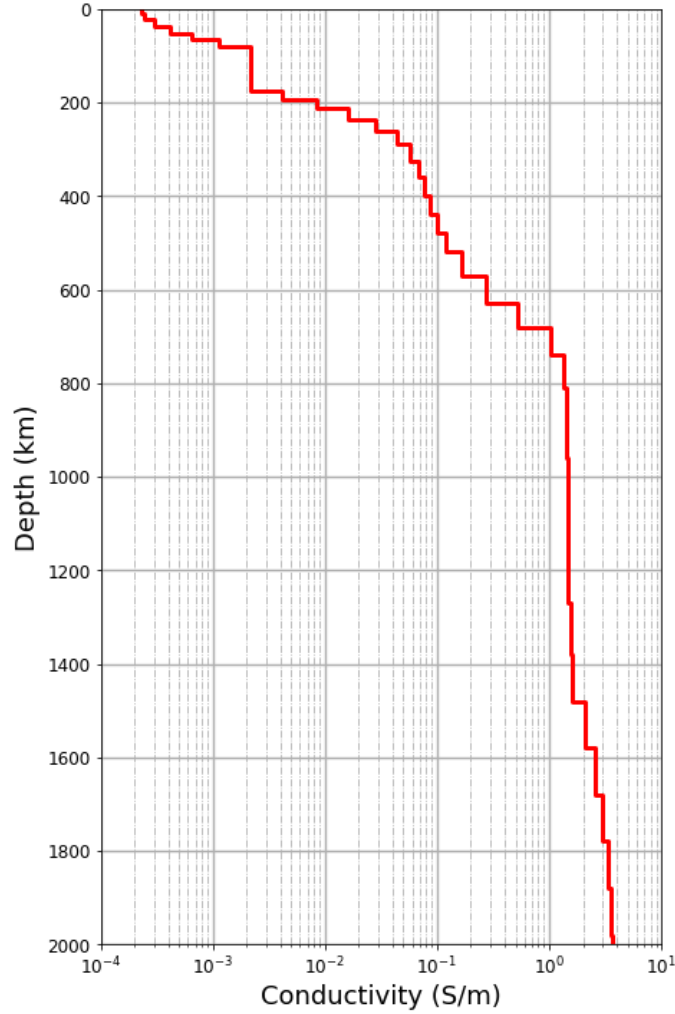


Figure 4.3: 1-D global conductivity model derived by GRAYVER *et al.* (2017) from the joint inversion of magnetospheric and ocean tidal magnetic signals, used as the background section in the modellings executed in this study.

coordinates with resolution of 1×1 arc min, where 1 arc min corresponds to 1.86 km at the equator. To create Gan observatory bathymetry model, data from the General Bathymetry Chart of the Oceans (GEBCO) 2019 was used, which has 15×15 arc sec horizontal resolution (GEBCO, 2019). Bathymetry is converted to Cartesian coordinates by the use of a Transverse Mercator map projection (ORDINANCE, 2016) and then linearly interpolated in a regular grid with $1 \text{ km} \times 1 \text{ km}$ horizontal resolution. Horizontally, we parameterize bathymetry in 356 horizontal cells with 1 km length, as in SAMROCK and KUVSHINOV (2013). Vertically, we assume that the 3-D anomaly lies between zero sea level and the maximum depth of bathymetry data and discretize it ten 100 m layers from the surface down to 1000 m depth. From 1000 m until the maximum bathymetry, the anomaly model is discretized in 500 m layers.

Global monthly oceanic conductivity are depth-averaged accordingly to the afore-

mentioned vertical layers. We use 2015 December oceanic electrical conductivity to model the OIE (Fig. 4.4). It can be observed that oceanic conductivity decreases with increasing depths and for depths larger than 1500 m it is approximately equal to 3.2 S/m everywhere (e.g. TYLER *et al.*, 2017). Thus, we calculate regional oceanic conductivity by horizontally averaging global conductivity in a $3^\circ \times 3^\circ$ squared region centered at each observatory and incorporate it into the top 2000 m depth. At deeper layers, oceanic conductivity is set to 3.2 S/m (Fig. 4.5). Furthermore, for each observatory we create a second model incorporating constant oceanic conductivity equal to 3.2 S/m in all vertical layers, as did in previous studies (cf. MORSCHHAUSER *et al.*, 2019; SAMROCK and KUVSHINOV, 2013).

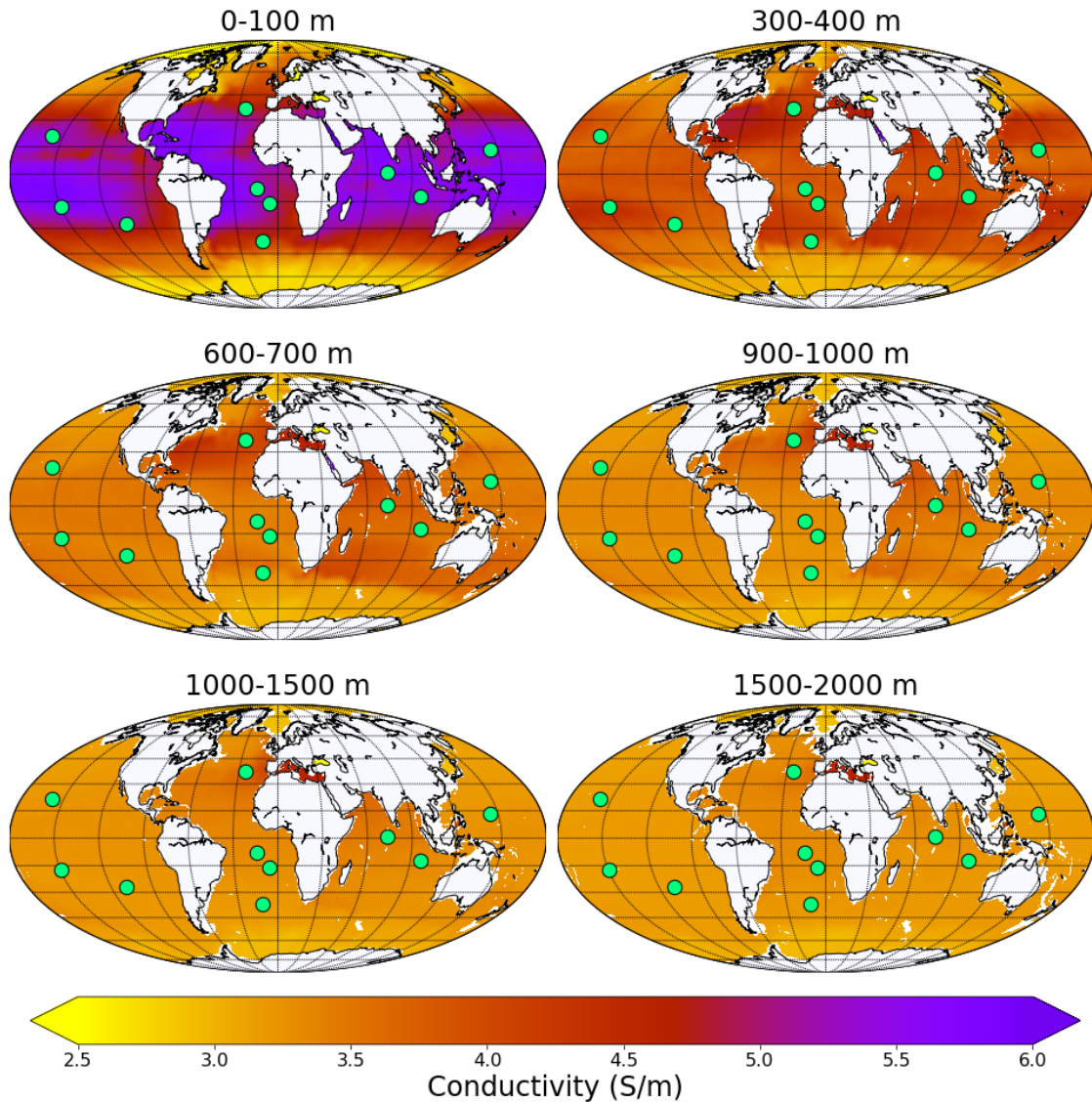


Figure 4.4: Calculated December global oceanic electrical conductivity, depth-averaged accordingly to vertical layers with depths of 0 m to 100 m, 300 m to 400 m, 600 m to 700 m, 900 m to 1000 m, 1000 to 1500 m and 1500 to 2000 m. Green circles represent island observatories used in this study.

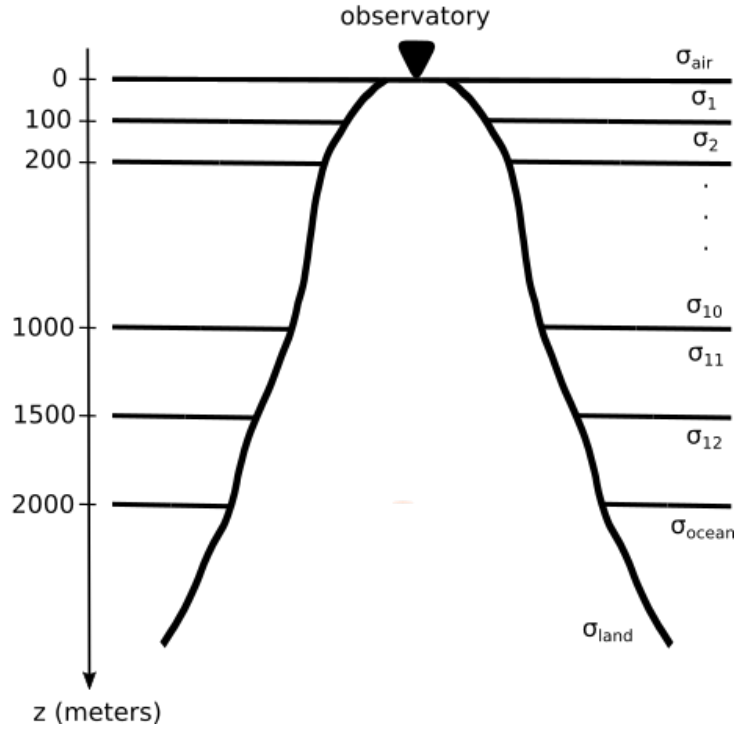


Figure 4.5: Vertical parameterization of the models used in this study. σ_{air} is the conductivity of the air, σ_1 to σ_{12} are the vertical layers where monthly depth-varying electrical conductivity are incorporated, σ_{ocean} is the deep (below 2000 m) ocean conductivity and σ_{land} is the continental landmass conductivity.

Continental landmass conductivity is set to 0.01 S/m and air conductivity is assumed to be negligible. Conductivity in border cells (located in the limit region between continental landmass and ocean) is calculated by the vertical integration of conductivity from each layer contained inside the cell. Topography is not included in models.

4.2.2 Calculation of Global Oceanic Electrical Conductivity

Monthly oceanic electrical conductivity is calculated from the Coriolis oceanographic data set for Re-Analysis (CORA5.0 CABANES *et al.*, 2013), provided by the Copernicus Marine Environment Monitoring Service. The data sets used consist of global monthly mean seawater temperature and salinity fields from 1990 to 2016 and distributed on a 0.5×0.5 horizontal grid and on 152 vertical layers between the sea surface and down to 2000 m. Oceanic conductivity is calculated from the aforemen-

tioned fields using the Gibbs-Seawater equation (?) with the conductivity function of the TEOS-10 toolbox (IOC, 2010). Oceanic pressure used in this calculation was approximated as $p \approx h$, where h is the depth of an specified data point. More details on the oceanographic data sets and calculation of corresponding global oceanic electrical conductivity can be found in PETEREIT *et al.* (2019).

4.2.3 3-D EM Modelling

The conductivity model, constructed as described in the previous section, is used as an input in PGIEM2G (KRUGLYAKOV and KUVSHINOV, 2018). This 3-D cartesian solver is based on a volume integral equation method and written in FORTRAN and C# programming languages. It supports the use of high-order polynomial basis and massive parallelization. Modellings were run in ETH-Zürich Euler supercomputer.

The code outputs real and imaginary parts of the x , y and z components of electric and magnetic fields linearly polarized in x and y directions, at each surface cell of the model. Tippers are then calculated by solving a linear system composed of a pair of Eq. 3.7 for modelled linearly polarized magnetic field components, i.e.

$$\begin{bmatrix} B_x^1 & B_y^1 \\ B_x^2 & B_y^2 \end{bmatrix} \begin{bmatrix} T_x \\ T_y \end{bmatrix} = \begin{bmatrix} B_z^1 \\ B_z^2 \end{bmatrix}; \quad (4.4)$$

where the superscripts 1 and 2 correspond to field components with x and y linear polarizations, respectively. The code to construct and solve this linear system was written in Python language by the author of this thesis.

Chapter 5

Results

This dissertation is divided in two parts: (i) a modelling study, in which tippers were modelled using 3-D conductivity models of island observatories in order to analyze the effects of depth and time varying oceanic electrical conductivity; and (ii) an experimental study, in which tippers were calculated using a global distribution of INTERMAGNET observatories to analyze the geographical and seasonal dependencies of their components. Those are explained in the following sections.

5.1 Modelling Study

Eight INTERMAGNET registered island magnetic observatories were used in this study (Fig. 5.1). Furthermore, we included data from St. Helena (SHE) and unpublished data from Santa-Maria/ Azores (SMA) observatories, both operated by GFZ-Potsdam since 2009 and 2018, respectively. More details on the magnetic observatories used in this study are presented on Table 5.1

5.1.1 Effects of Depth-Varying Oceanic Conductivity

Modelling results for all magnetic observatories are presented in Figs. 5.2 to 5.11. In all of the figures, Plot (a) presents the top view of bathymetry model, where the corresponding observatory is located in the centre of this plot. The dashed line indicates the location of the west-east bathymetry profile shown in Plot (b). Plot (c) presents calculated regional depth-varying (purple line) and constant (orange line) oceanic conductivity profiles down to 2 km, which are extracted from the global data set shown in Figure 5.1. Plots (d) to (g) present $\Re T_x$, $\Re T_y$, $\Im T_x$ and $\Im T_y$ tipper components, respectively. Red and orange curves correspond to tippers modelled incorporating depth-varying and constant oceanic electrical conductivity, respectively (see corresponding profiles in Plot c) and blue curve represent observations.

Table 5.1: Information on the magnetic observatories used in this study: IAGA codes, names, latitudes (θ), longitudes (ϕ), where superscripts GC and GM respectively correspond to geocentric and geomagnetic coordinates, their starting date of operations in INTERMAGNET and period of time series used to estimate tippers. Observatories with an asterisk (*) are, as of date, not registered to INTERMAGNET. Geomagnetic coordinates were calculated using IGRF-12, epoch 2015

Code	Name	θ^{GC}	ϕ^{GC}	θ^{GM}	ϕ^{GM}	Starting Date (INTERMAGNET)	Length of Time Series
ASC	Ascension Island	7.95	-14.38	-2.77	57.48	2003	01/01/2014 – 31/12/2014
CKI	Cocos-Keeling Islands	12.10	-96.84	-21.56	168.92	2013	01/01/2015 – 30/06/2015
GAN	Gan	0.69	73.15	-8.64	145.33	2013	01/01/2017 – 31/12/2017
GUA	Guam	13.59	144.87	5.8	216.51	1991	01/01/2016 – 31/12/2016
HON	Honolulu	20.32	-158	21.65	270.85	1991	01/01/2015 – 30/09/2015
IPM	Easter Island	-27.2	-109.42	-19.17	325.61	2010	01/01/2013 – 31/12/2013
PPT	Pamatai	-17.57	-149.58	-15.05	285.79	1991	01/01/2015 – 31/12/2015
SHE	St. Helena	-15.96	-5.75	11.78	64.24	2009*	01/01/2013 – 30/06/2013
SMA	Santa Maria/Azores	36.99	-25.13	43.21	53.57	2018*	01/07/2018 – 31/10/2018
TDC	Trista da Cunha	-37.07	-12.31	-31.70	54.76	2010	01/01/2015 – 30/09/2015

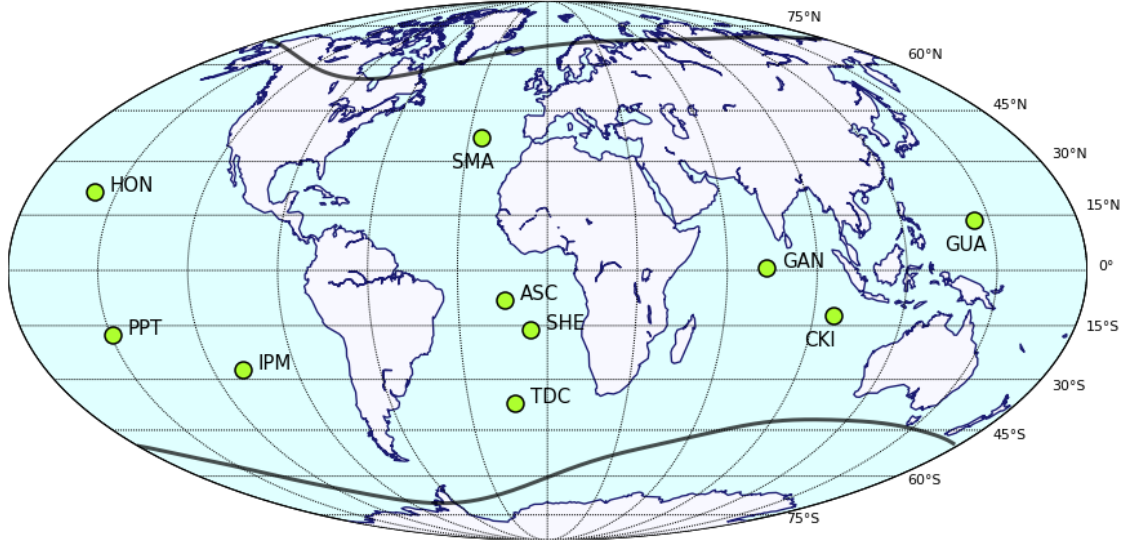


Figure 5.1: Magnetic observatories used in this study (green circles) and northern and southern Auroral Electrojets. Observatories information can be found in Table 5.1.

Plots (h) and (i) respectively present modelled T_x and T_y components OIE (ΔT_x and ΔT_y , respectively, and both represented as dashed red lines), defined as

$$\Delta T_i = \sqrt{(\Re T_i^{dv} - \Re T_i^{ct})^2 + (\Im T_i^{dv} - \Im T_i^{dv})^2} \quad (5.1)$$

where superscripts "dv" and "ct" correspond to tippers calculated using depth-varying and constant conductivity, respectively, and $i \in [x, y]$. Thus, the modelled OIE represents the part of tippers that is entirely due to oceanic electrical conductivity variations. The value of 0.025, represented as dashed gray lines, is used as a

threshold to define when the ocean effect needs to be accounted for in tippers modelling since this value is traditionally used as an error floor in tipper inversions (e.g. BEDROSIAN and FEUCHT, 2014; MORSCHHAUSER *et al.*, 2019; RAO *et al.*, 2014; TIETZE and RITTER, 2013; YANG *et al.*, 2015).

In all observatories, the OIE becomes observable (larger than the threshold) at periods larger than approximately 1 sec. This effect is observable (larger than the threshold) in all observatories except for ASC (Fig. 5.2, IPM (Fig. 5.7) and SHE (Fig. 5.9), where it is negligible for all periods. At other observatories, the OIE varies with location, period and component (T_x or T_y) at varying degrees. The maximum effects are observed at GAN (Fig. 5.4) and HON (Fig. 5.6), where it reaches the values of 0.9 and 0.12 for T_x and T_y components, respectively.

Variations of oceanic conductivity are restricted to the top 1 km depth in most observatories, except for GAN and SMA (Fig. 5.10) where they are observed down to 2 km. Thus, variations of the OIE with respect to periods and components appear to depend on local bathymetry distributions around observatories. It is observable at the $10^1 - 10^2$ sec period range at CKI (Fig. 5.3), GAN and TDC and for periods larger than 1 sec at GUA (Fig. 5.5), HON, PPT and SMA.

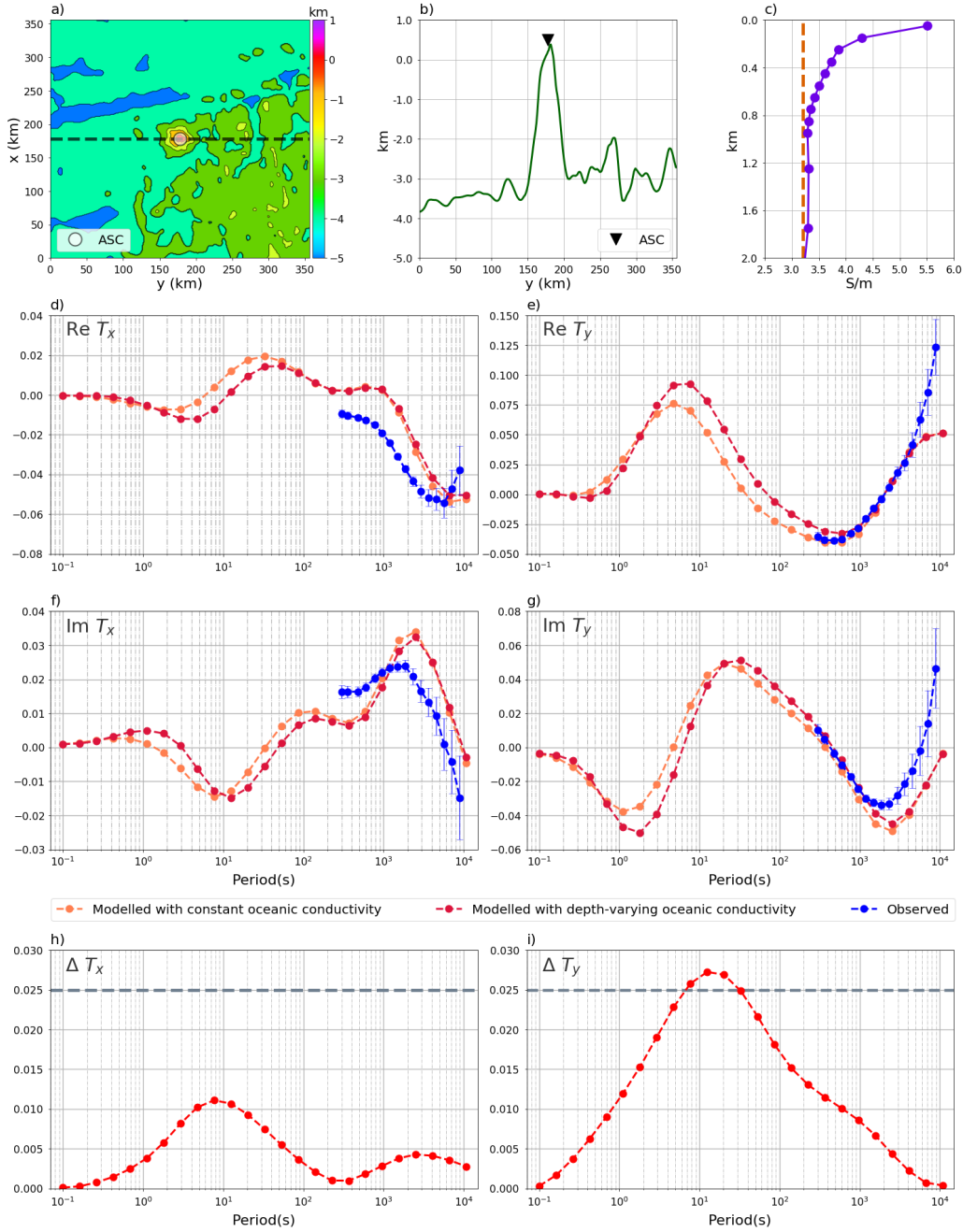


Figure 5.2: Ascension Island observatory (ASC) bathymetry model, regional oceanic electrical conductivity profiles, modelled and observed tippers and modelled ocean induction effects (OIE). (a) presents the top view of the bathymetry model, where the dashed line indicates the profile in (b), presenting the west-east bathymetry profile across the modelling domain. (c) presents regional depth-varying (purple) and constant with respect to depth (orange) oceanic conductivity electrical profiles, extracted from the dataset shown in Fig. 5.1. (d) to (g) present modelled (orange and red curves) and observed (blue curves) tipper components: $\Re T_x$, $\Re T_y$, $\Im T_x$, $\Im T_y$. Orange and red curves correspond respectively to tippers modelled incorporating constant and depth-varying oceanic electrical conductivity shown in Fig. 5.2 c. (h) and (i) present modelled T_x and T_y components ocean effects as red curves and the threshold of 0.025 as grey lines.

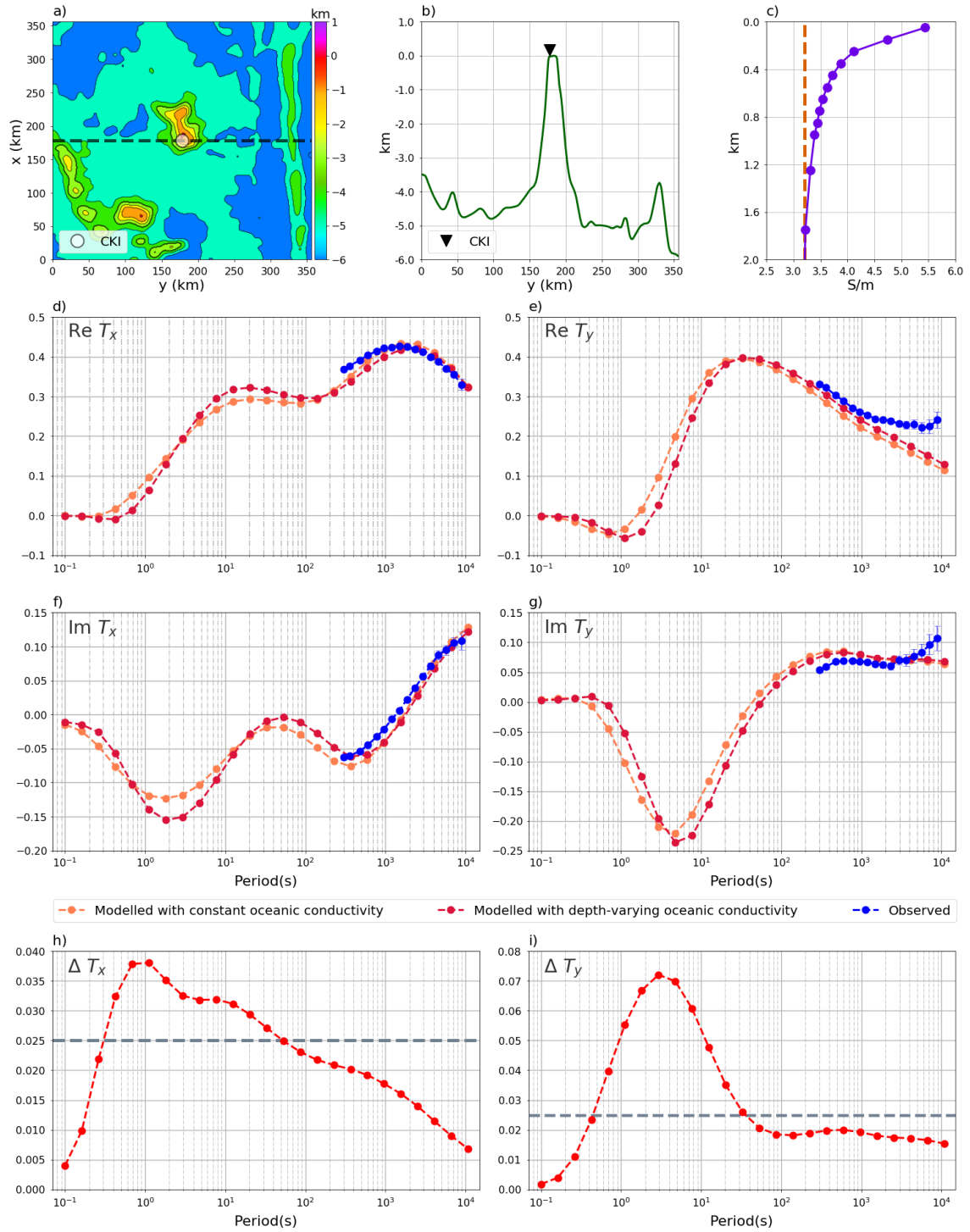


Figure 5.3: Same as Fig. 5.2, but for Cocos-Keeling Islands observatory (CKI) .

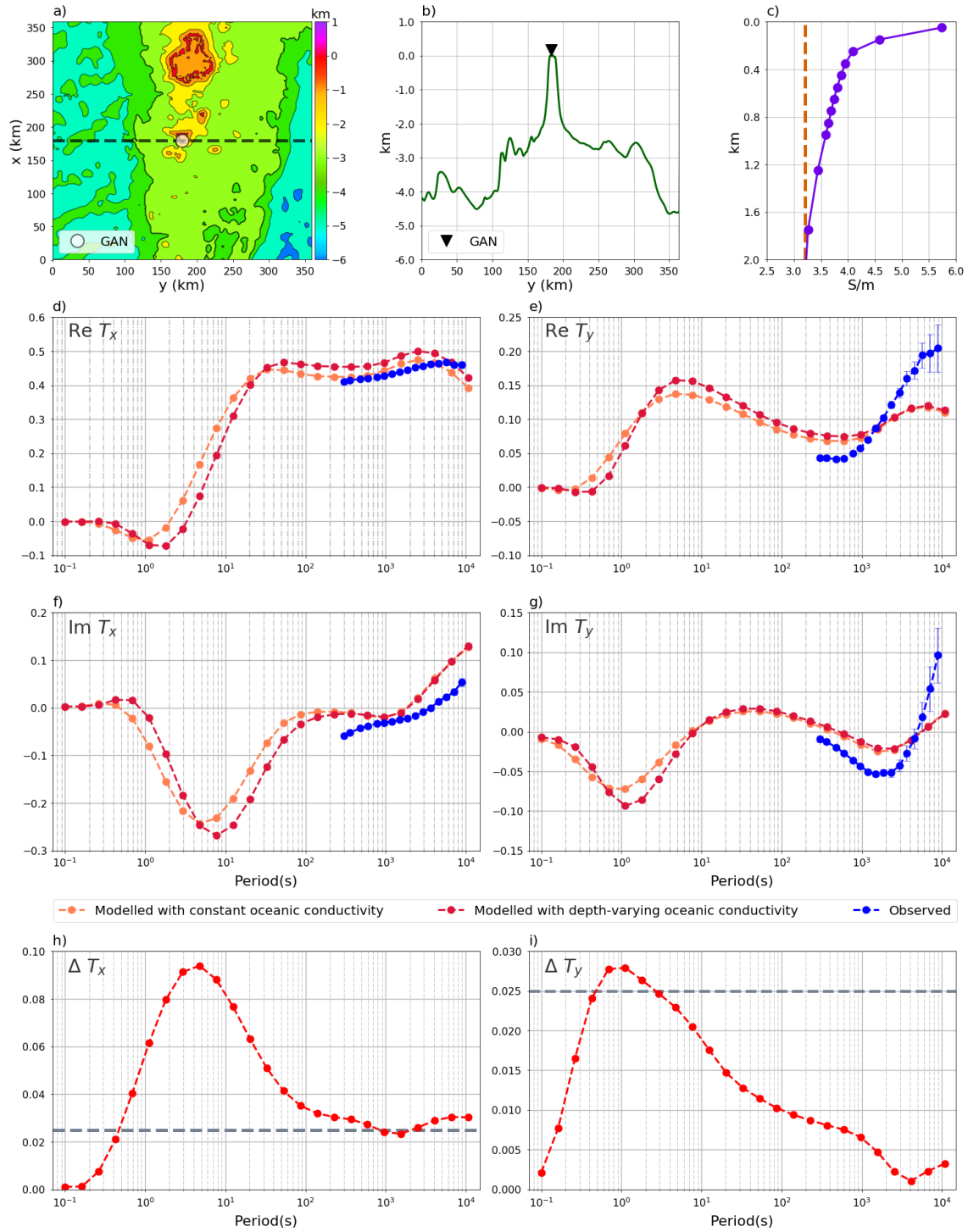


Figure 5.4: Same as Fig. 5.2, but for GAN observatory (GAN).

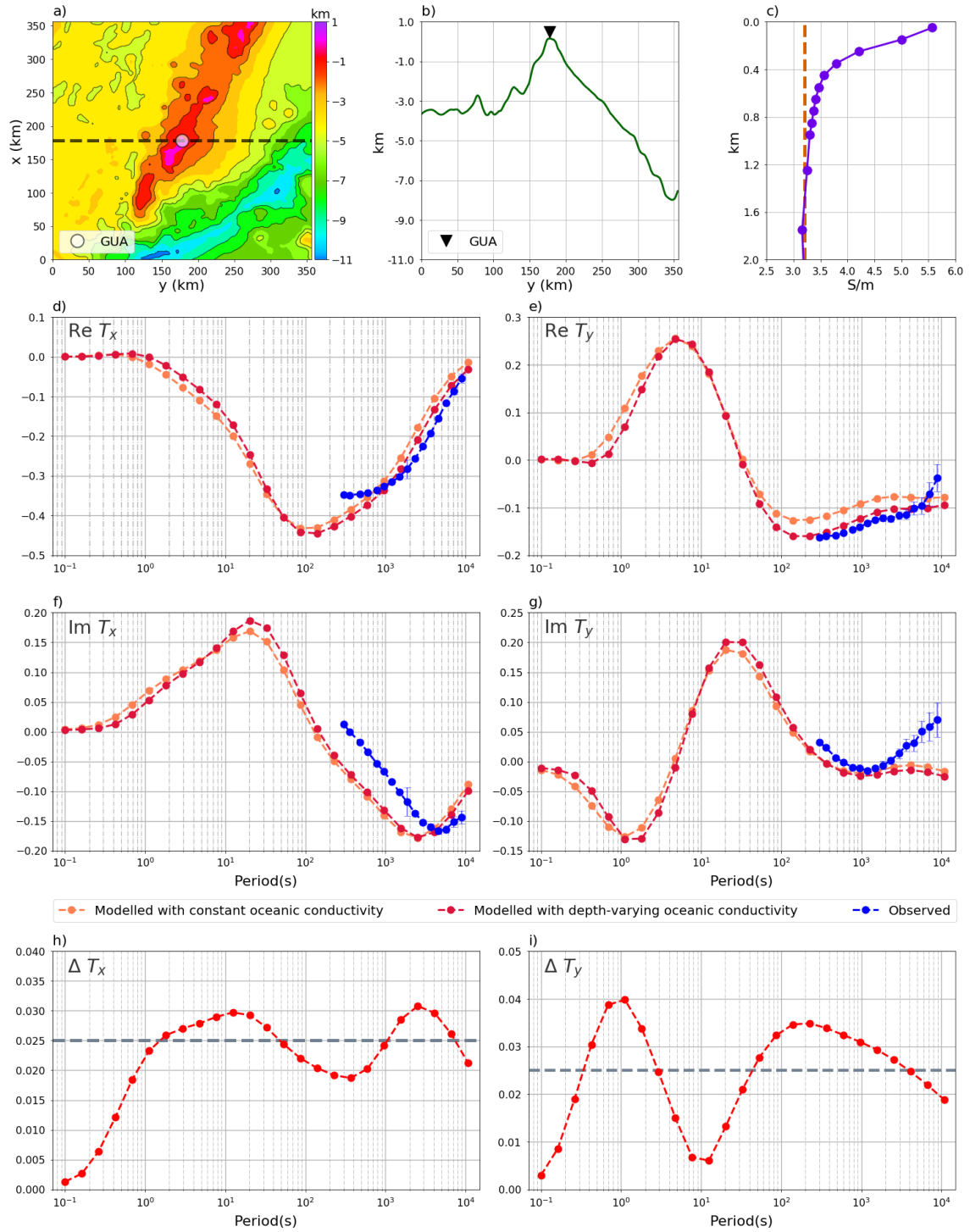


Figure 5.5: Same as Fig. 5.2, but for Guam observatory (GUA).

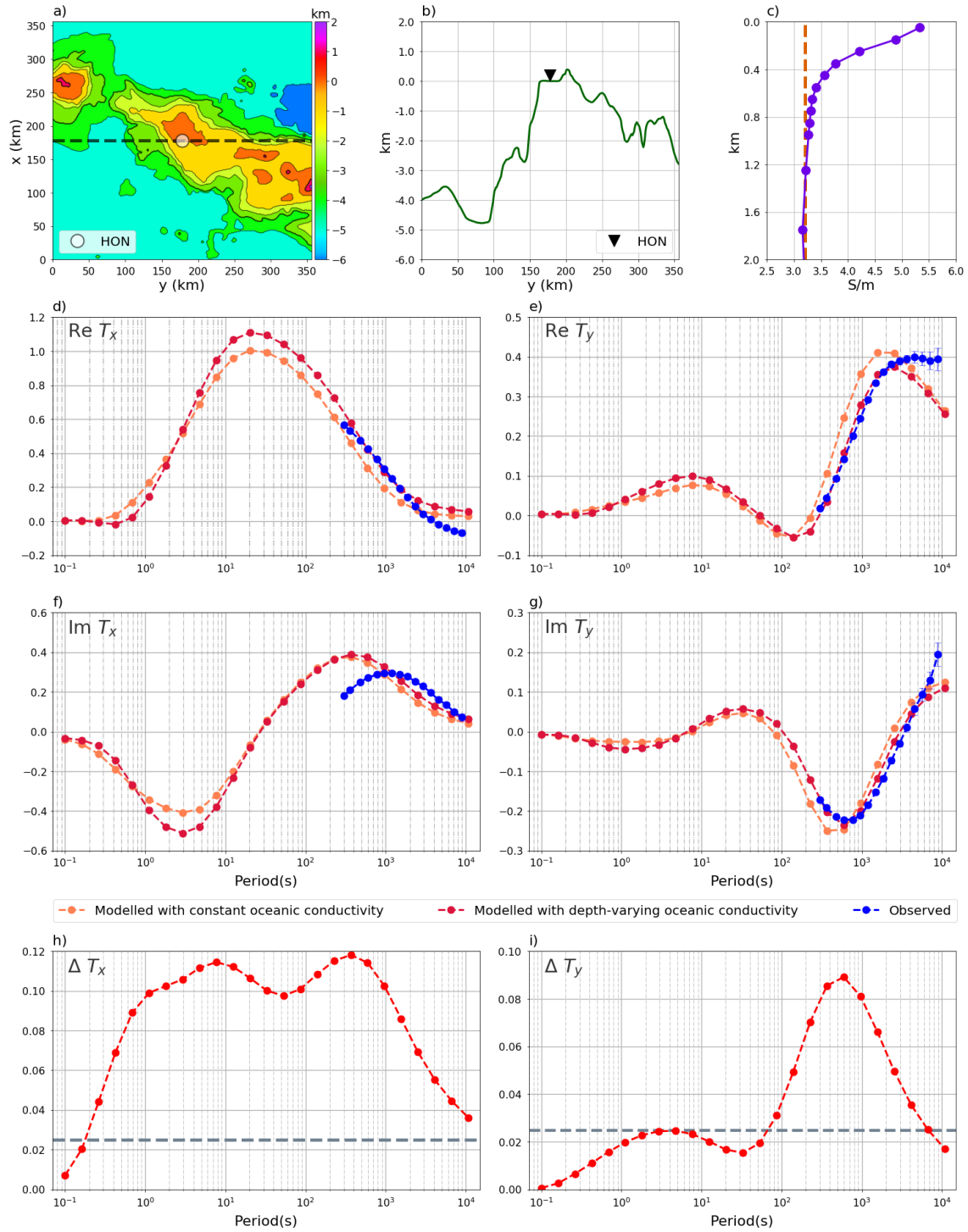


Figure 5.6: Same as Fig. 5.2, but for Honolulu observatory (HON).

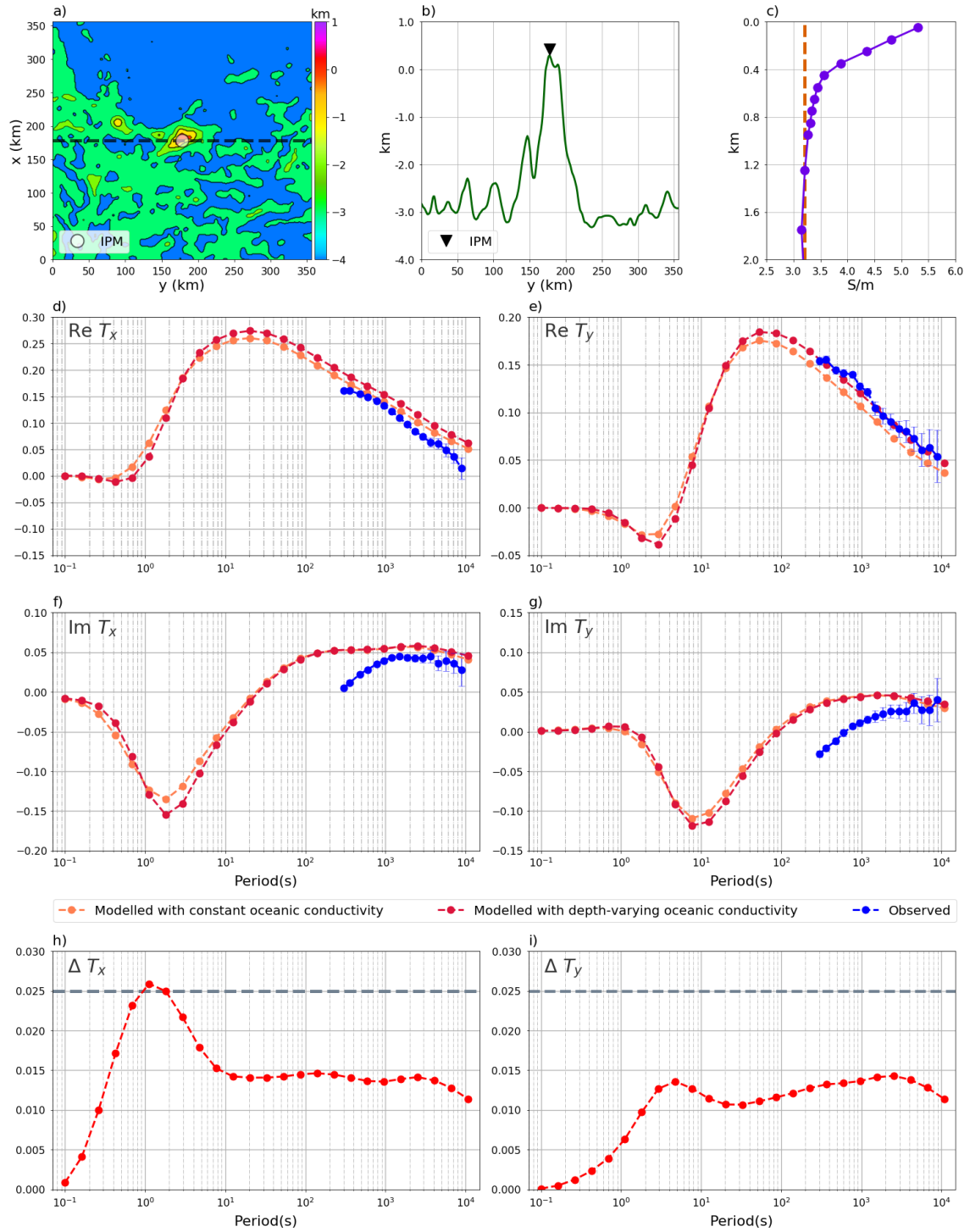


Figure 5.7: Same as Fig. 5.2, but for Easter Island observatory (IPM).

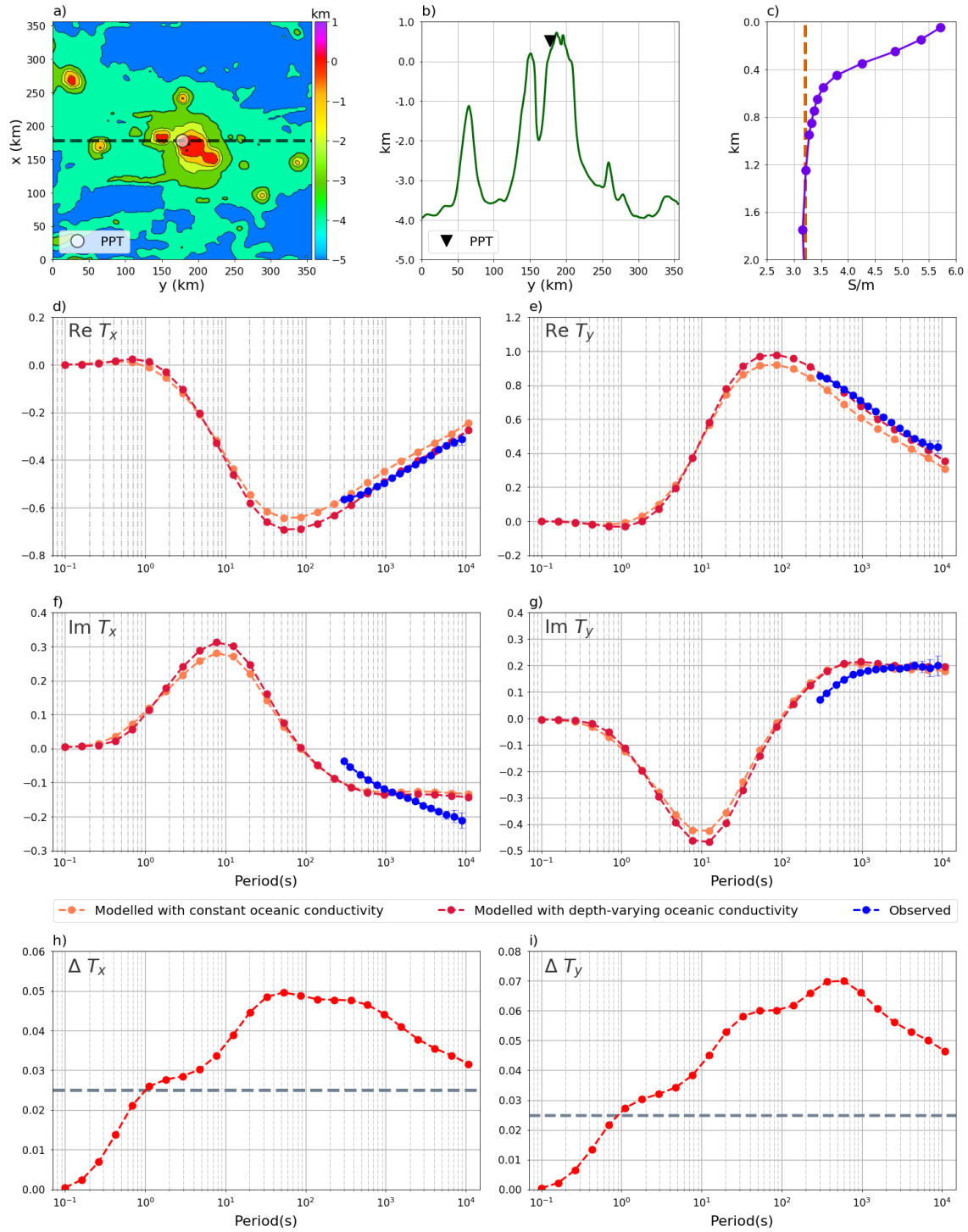


Figure 5.8: Same as Fig. 5.2, but for Pamatai observatory (PPT).

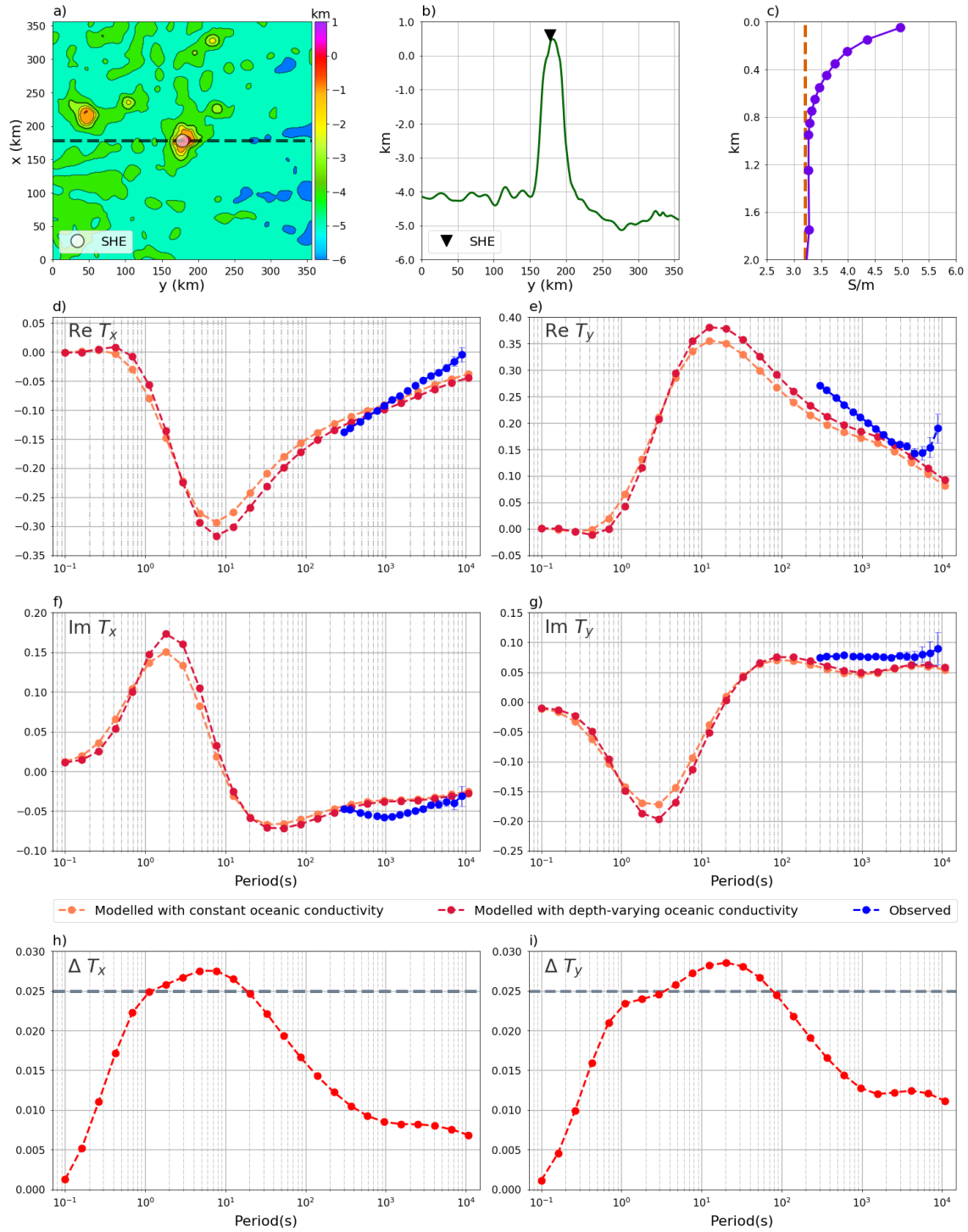


Figure 5.9: Same as Fig. 5.2, but for St. Helena observatory (SHE).

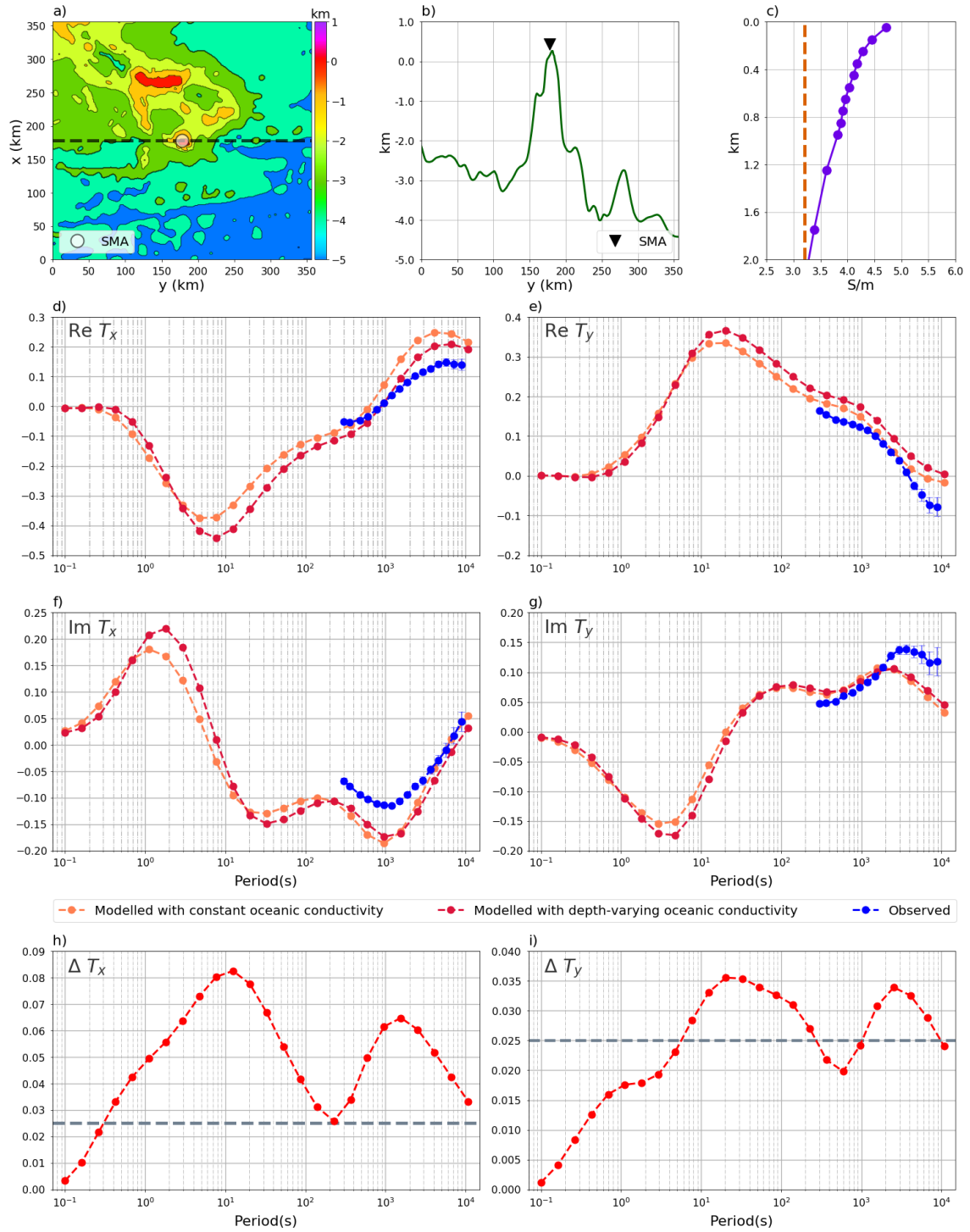


Figure 5.10: Same as Fig. 5.2, but for Santa-Maria/Azores observatory (SMA).

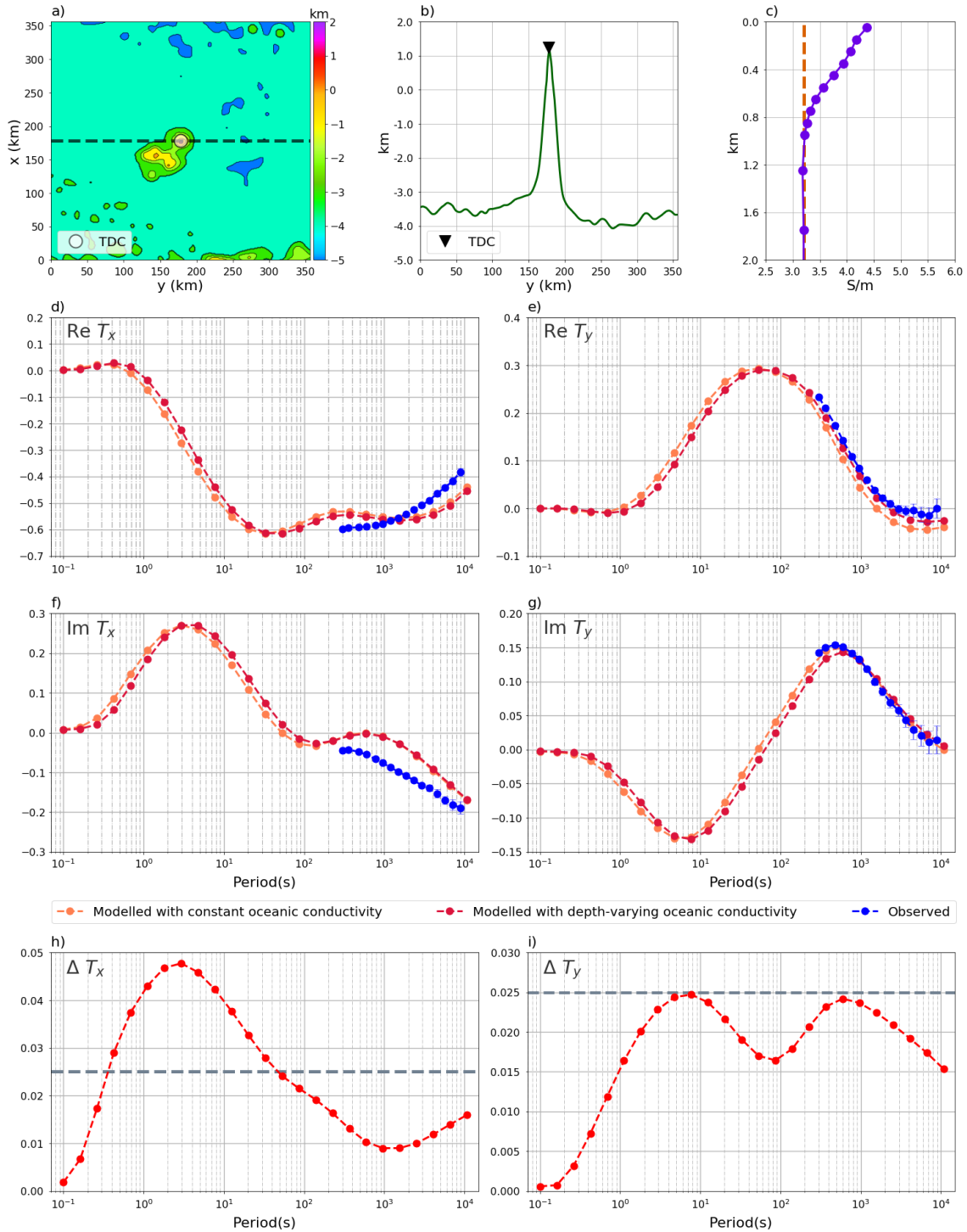


Figure 5.11: Same as Fig. 5.2, but for Tristan da Cunha observatory (TDC).

5.1.2 Effects of Time-Varying Oceanic Electrical Conductivity

Temporal variations of tippers due to time-varying oceanic conductivity are calculated by the absolute difference between tippers modelled incorporating December and June oceanic electrical conductivity, i.e.

$$\widehat{\Delta T}_i = \sqrt{(\Re T_i^{dec} - \Re T_i^{jun})^2 + (\Im T_i^{dec} - \Im T_i^{jun})^2} \quad (5.2)$$

where $\widehat{\Delta T}_i$ is the modelled temporal variability of the corresponding tipper component, with $i \in [x, y]$. Superscripts "dec" and "jun" correspond to December and June conductivity models, respectively. Thus, modelled variabilities correspond to variations in tipper components due to electrical conductivity differences between the aforementioned months (Fig. 5.12).

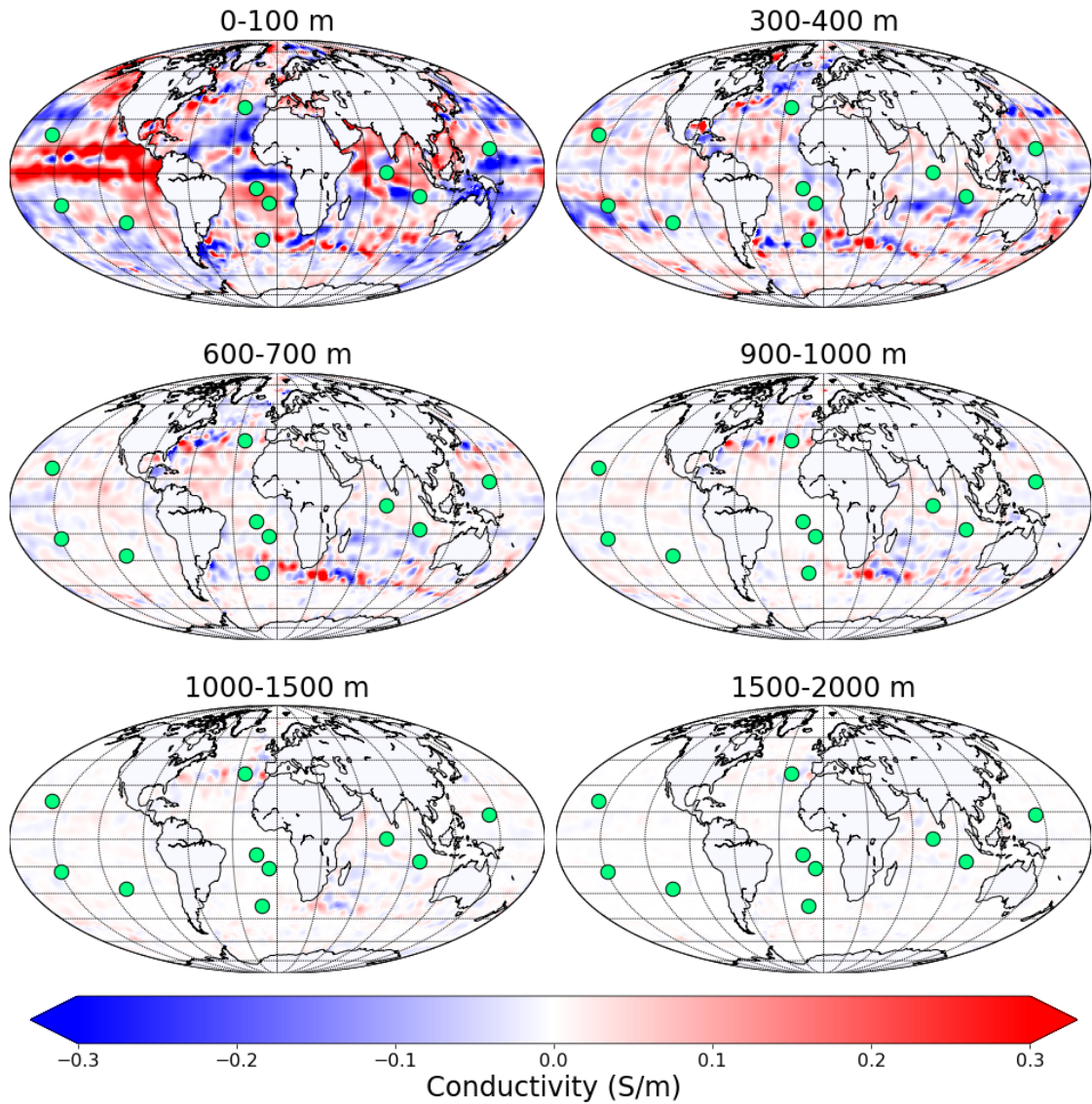


Figure 5.12: Difference between December and June oceanic electrical conductivity, depth-averaged accordingly to vertical layers with depths of 0 m to 100 m, 300 m to 400 m, 600 m to 700 m, 900 m to 1000 m, 1000 to 1500 m and 1500 to 2000 m.

T_x and T_y components modelled and observed variabilities are presented in Figs. 5.13 and 5.14, respectively. For simplicity of presentation, only results for six periods linearly spaced in the 10^{-1} to 10^4 s are shown. Maximum observed vari-

abilities vary from 0.06, at 300 sec, to 0.24 at 9600 sec. Modelled variabilities are of three orders less than observations, having maximum value of 0.003. Therefore, from this modelling study, it can be concluded that the influence of temporal variations of oceanic electrical conductivity on temporal variations of tippers is negligible.

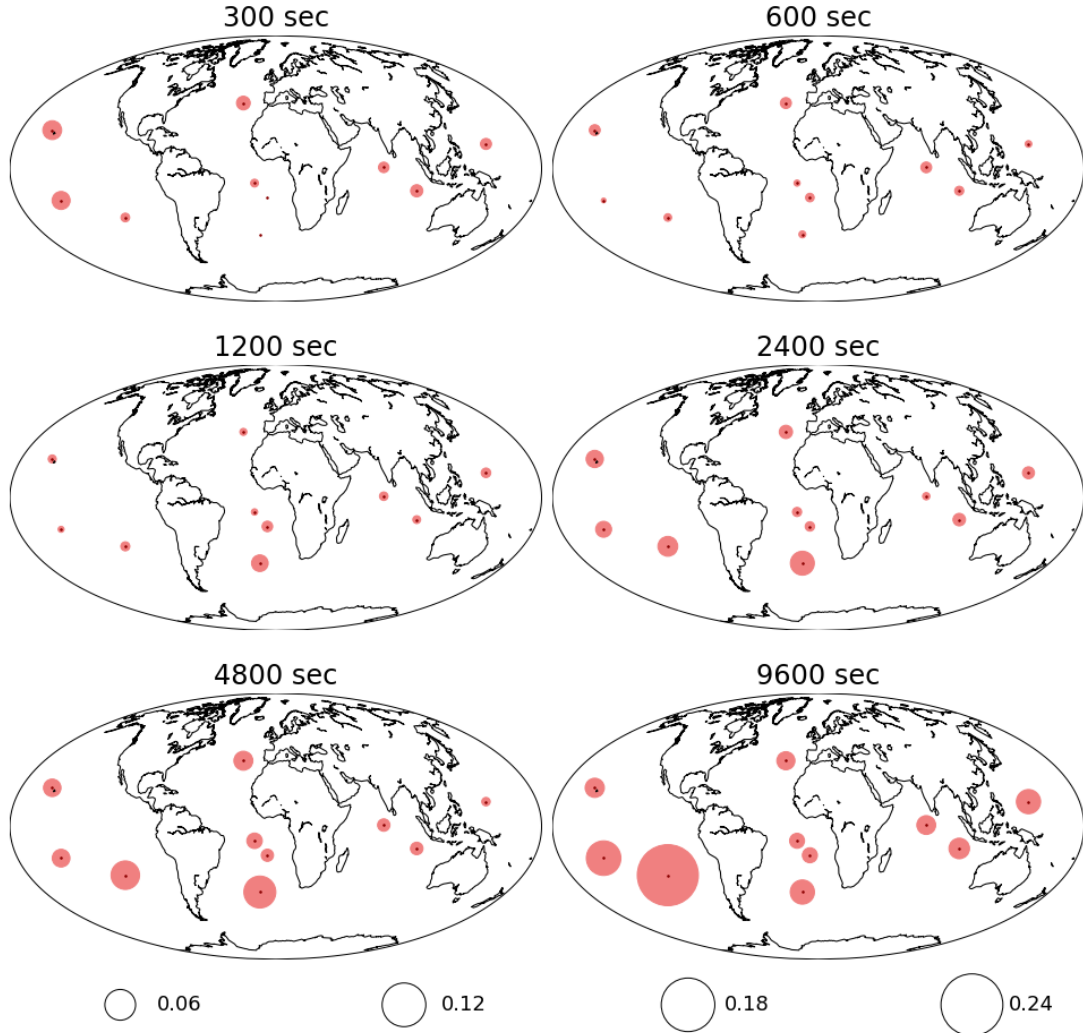


Figure 5.13: Modelled (dark red circles) and observed (light red circles) T_x component variability, for periods of 300 sec, 600 sec, 1200 sec, 2400 sec, 4800 sec and 9600 sec. The size of circles indicates four ranges of amplitudes: 0.06, 0.12, 0.18 and 0.24.

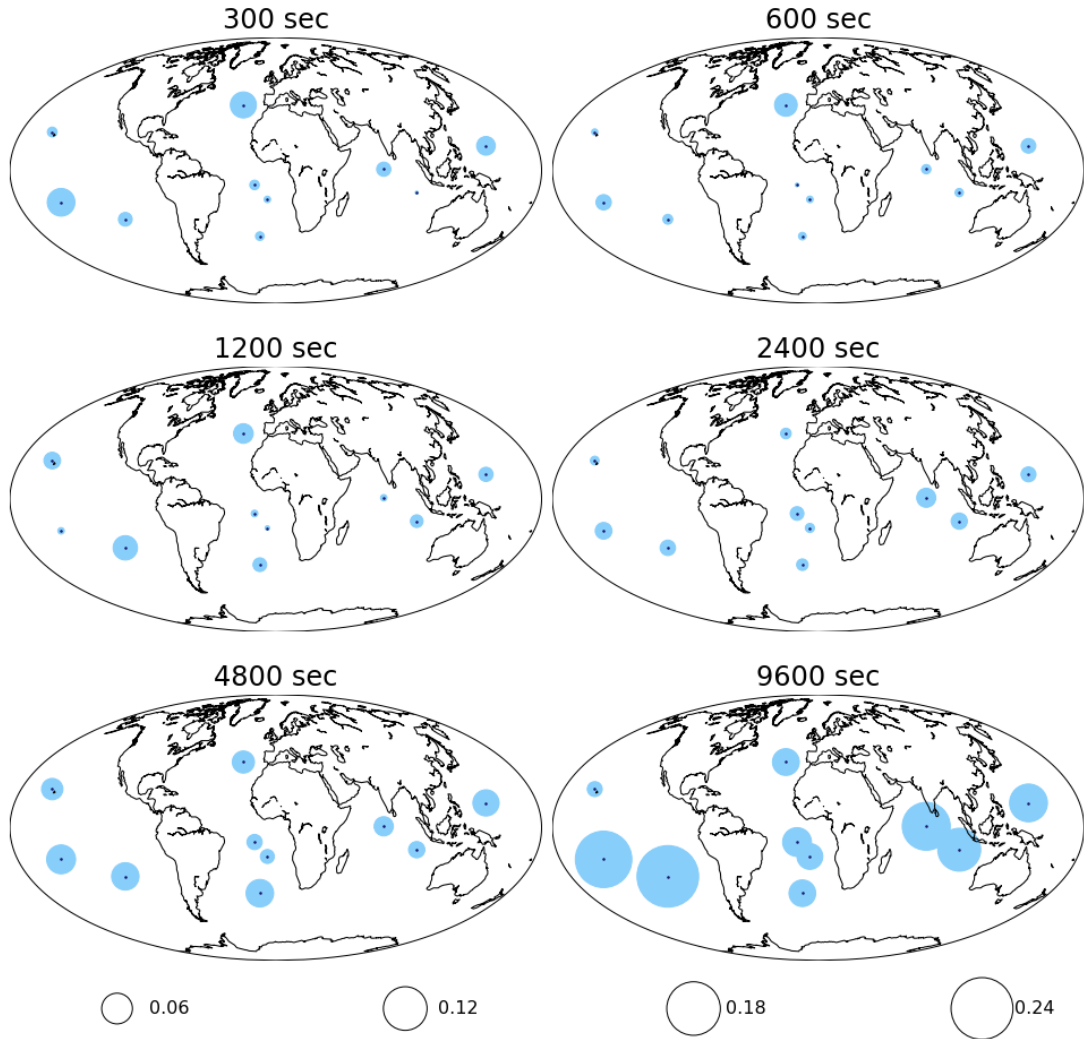


Figure 5.14: Modelled (dark blue circles) and observed (light blue circles) T_y component variability, for periods of 300 sec, 600 sec, 1200 sec, 2400 sec, 4800 sec and 9600 sec. The size of circles indicates four ranges of amplitudes: 0.06, 0.12, 0.18 and 0.24.

5.2 Experimental Data Study

Observatories used in the experimental part of this study are presented in Figure 5.15. Observatories under the Auroral Electrojets influence or with significant data gaps (more than 3 days) were excluded from this analysis. In total, tippers were calculated for 52 magnetic observatories.

To account for seasonal variations, calculated variabilities (see Section 4.1) were grouped in the three Lloyd Seasons of the year, defined as:

- D: November, December, January, February;
- E: March, April, September, October;

- J: May, June, June , August.

Therefore, D and J seasons correspond to December and June solstices, periods when insolation is higher in the northern and southern hemispheres, respectively. The E seasons correspond to the equinox, when insolation is the same in both hemispheres. Errors bars were calculated from the linear propagation of the monthly experimental tippers errors.

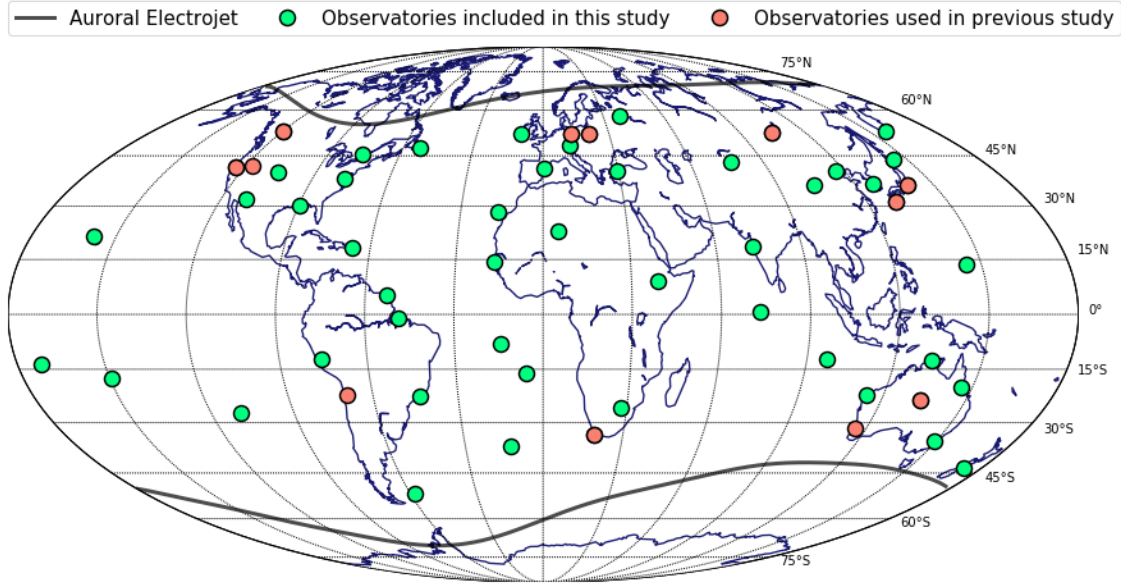


Figure 5.15: Magnetic observatories used in the experimental part of this study. Red circles represent observatories analyzed in ARAYA VARGAS and RITTER (2016), green circles represent observatories included in this study and black lines represent the positions of the northern and southern Auroral Electrojets.

Calculated $\Re(T_x)$ variabilities are presented in Fig. 5.16 (a). Green dashed lines represent the ± 0.025 tipper amplitude, defined as a threshold to define regions where variabilities are large enough to be accounted for in modelling, given that this value is traditionally used as an error floor in EM inversions (BERDICHEVSKY and DMITRIEV, 2008). For all seasons, variabilities and errors increase with increasing periods. In the 300 sec to 1200 sec period range, variabilities in general are lower than the threshold in all latitudes, thus they are negligible in these periods. For 2400 sec, the seasonal modulations identified in ARAYA VARGAS and RITTER (2016) are observed in latitudes larger than 35° , characterized by negative and positive increases of D and J seasons variabilities, respectively, which in general exceed the threshold. Outside of this latitude range, these variations are negligible. In general, E season variabilities are negligible for EM modellings in all latitudes and periods. Furthermore, all seasons variabilities are negligible from -60° to -45° latitudes. Errors increase with increasing periods, particularly in 2400 sec. This is due to

violations of the plane wave assumption at long periods and to harmonics of the Sq (Solar quiet) current system SCHMUCKER (1999).

$\Im(T_x)$ variabilities (Fig. 5.16 b) present a similar geographical pattern as the $\Re(T_x)$ component, but with seasonal modulations with opposite polarization (positive and negative D and J seasons variabilities, respectively). These exceed the threshold only in latitudes larger than 35° and for periods starting from 1200 sec. Thus, seasonal variations of both T_x components are negligible in latitudes smaller than 35° . As in $\Re(T_x)$, E season variabilities amplitudes are negligible in all periods and latitudes, as all seasonal variations in the -60° to -45° latitude range.

To investigate the maximum part of tippers that may be due to seasonal variations, we calculated the difference between $\Re(T_x)$ D and J seasons variabilities (Fig. 5.17). For $\Re T_x$ (Fig. 5.17 a). These differences are negligible in the 300 sec to 1200 sec period range and in all latitudes. For 2400 s, these differences are larger than the threshold in latitudes larger than 35° , with maximum absolute amplitude of 0.1 in two observatories. $\Im(T_x)$ component variabilities (Fig. 5.17 b) present a similar geographical pattern, but with positive values and exceeding the threshold for periods of 1200 sec and 2400 sec, with maximum amplitudes of 0.12, at 2400 sec. Therefore, these differences need to be accounted for when comparing tippers measured in the aforementioned seasons and latitude ranges.

For the $\Re(T_y)$ component (Fig. 5.18 a), in all periods a few observatories present D and J seasons variabilities larger than the threshold from -35° to 35° latitudes. For 2400 sec, D and J seasonal modulations are observed in latitudes larger than 35° , having the same polarizations as in $\Re(T_x)$ (Fig. 5.16 a) but with smaller amplitudes. These modulations are not observed in other latitudes. Furthermore, in general E season variabilities are smaller than the threshold in all latitudes and periods, as all seasonal variations in the -60° to -45° latitude range.

$\Im(T_y)$ component variabilities are presented on Fig. 5.18 (b). For all periods and seasons, in general variabilities are smaller than the threshold. However, seasonal modulations are observed in 2400 sec, characterized by an increase of D season variabilities in the southern hemisphere and decrease in the northern hemisphere. Modulations are also observed during the J season, but with opposite polarization. Nevertheless, both have negligible effects for EM inversions. Furthermore, this is the only tipper component where no seasonal modulation effects are observed in latitudes larger than 35° .

Differences between D and J seasons variabilities $\Re(T_y)$ are presented in Fig. 5.19 (a). From periods of 300 sec to 600 sec variabilities are smaller than the threshold in all latitudes except in a few low latitude observatories. Starting from 1200 sec, amplitude of variabilities exceed the threshold in the -35° to 60° latitude range, but they are negative starting from 35° . Moreover, for all periods these differences

are smaller than the threshold in the -60° to -45° latitude range. For the $\Im(T_y)$ component, presented in Fig. 5.19 (b), those differences are relevant for inversions starting from periods of 1200 sec and 2400 sec, in the northern hemisphere. For both components, seasonal differences can have maximum amplitude of 0.10 in latitudes larger than 35° .

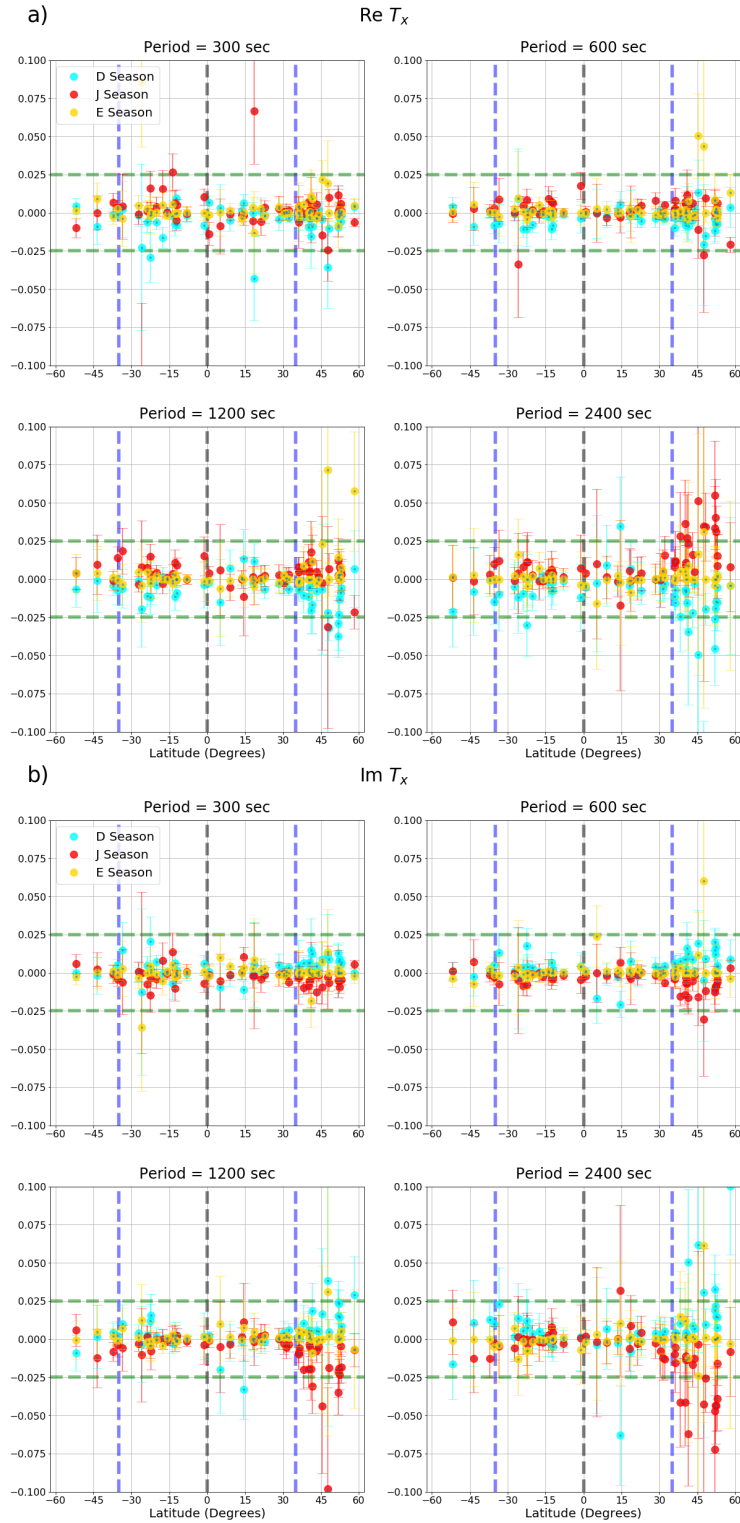


Figure 5.16: Global real (a) and imaginary (b) T_x component variabilities for periods of 300 s, 600 s, 1200 s, 2400 s, 4800 s and 9600 s. The blue, red and yellow circles represent D, J and E seasonal variabilities, respectively. Gray and blue dashed lines correspond to the geographic equator and $\pm 40^\circ$ latitudes, respectively. Green dashed lines represent the threshold defining the minimum tipper amplitudes with implications to EM inversion (± 0.025). The error bars are calculated for each period and season from the corresponding monthly tippers errors.

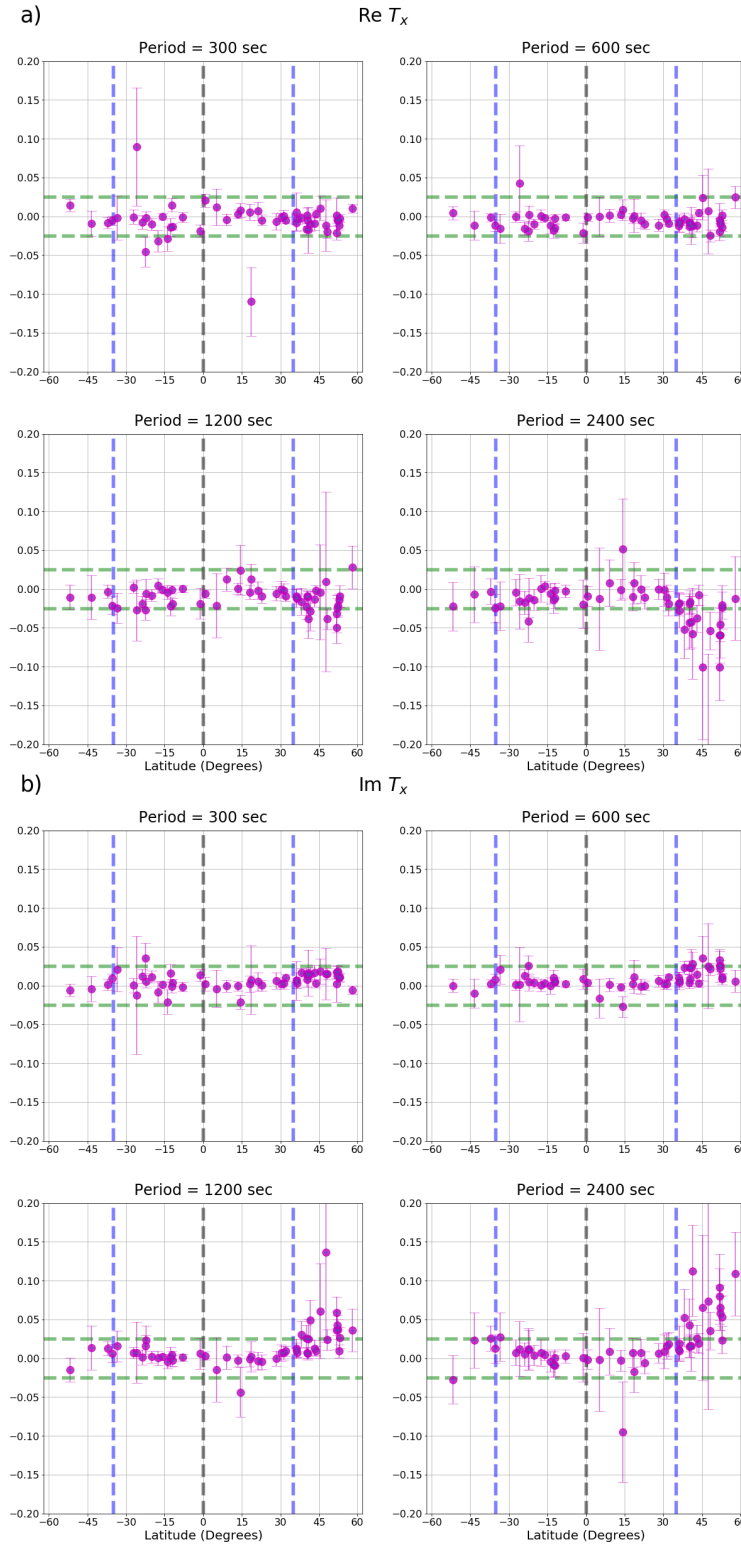


Figure 5.17: Difference between D and J real (a) and imaginary (b) T_x seasonal variabilities (purple circles) for periods of 300 s, 600 s, 1200 s, 2400 s, 4800 s and 9600 s. Gray and blue dashed lines correspond to the geographic equator and $\pm 40^\circ$ latitudes, respectively. Green dashed lines represent the threshold defining the minimum tipper amplitudes with implications to EM inversion (± 0.025). The error bars are calculated for each period and season from the monthly tippers errors.

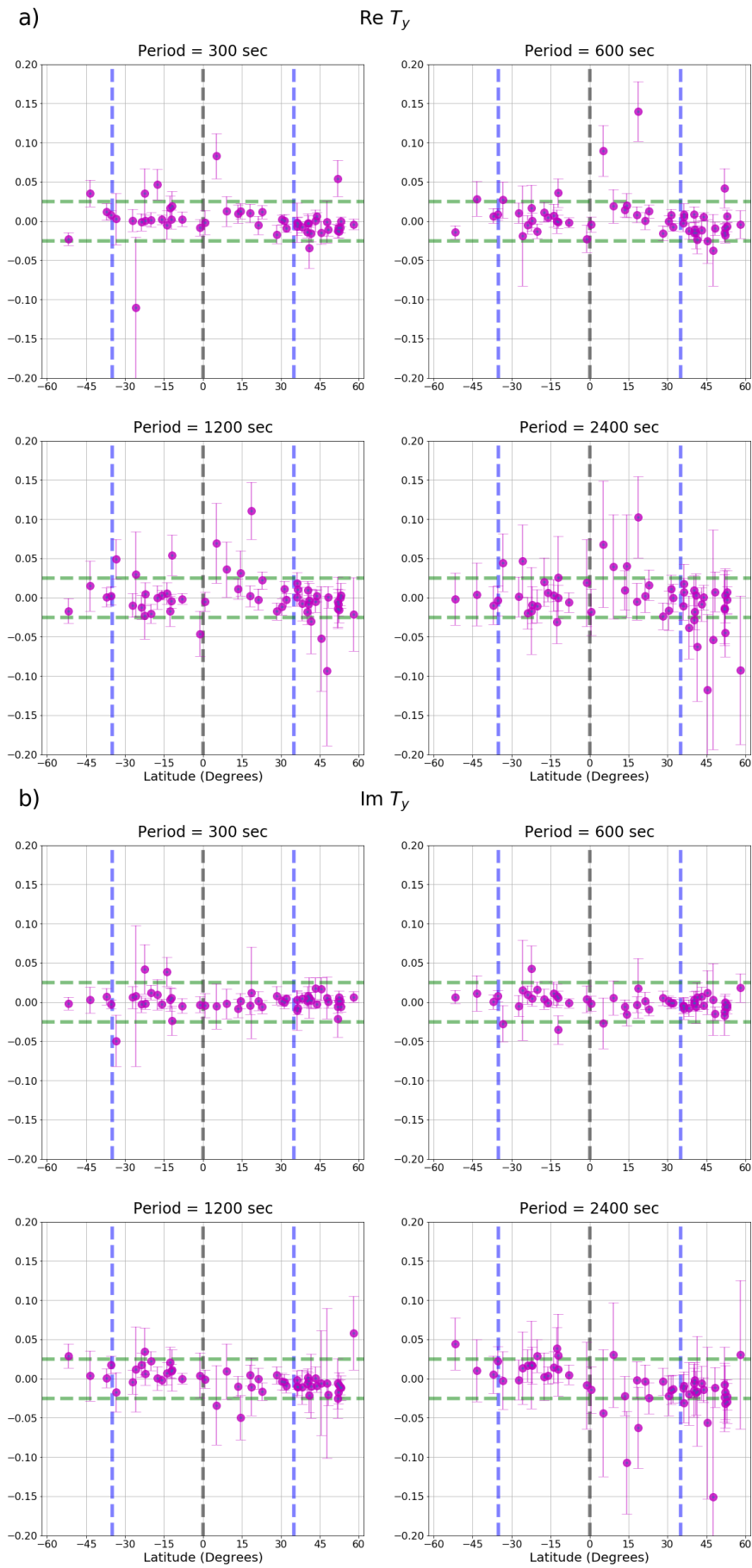


Figure 5.19: Same as Fig. 5.17, but for real (a) and imaginary (b) T_y seasonal variabilities.

Chapter 6

Conclusions

In this study, I collaborated with two different international research institutes (ETH-Zürich and GFZ-Potsdam) to investigate anomalous effects on tippers measured in magnetic observatories. In the modelling part of this study, I analyzed the effects of realistic oceanic electrical conductivity variations, calculated from global temperature and salinity data, on tippers measured in island observatories. I incorporated temporal and depth-varying oceanic conductivity variations into 3-D conductivity models constructed from bathymetry data and modelled this effect using a 3-D integral equation EM solver. This is the first study that has successfully modelled tippers incorporating realistic oceanic electrical conductivity.

I demonstrated that, in some observatories, part of tipper components is due to depth-varying oceanic conductivity variations. Amplitude and period ranges of the ocean effect depend on the oceanic conductivity and bathymetry of the region. In most observatories, this effect is modelled by oceanic conductivity variations in the first 1 km depth, and deeper variations are negligible. However, in three observatories (CKI, GAN and SMA) conductivity variations are observed up to 2 km depth. Moreover, in most observatories incorporation of depth-varying oceanic conductivity improved the fit to observed tippers, in comparison with tippers calculated using constant oceanic conductivity (as in previous modelling studies). Therefore, it is recommended to use realistic oceanic conductivity when modelling tippers in oceanic sites if this data is available and trustworthy.

I also showed that, over the time, monthly variations of oceanic conductivity have a negligible effect on variability of tippers components, in the 10^{-1} to 10^4 seconds period range. Therefore, temporal variations of tippers observed in island observatories are most probably due to the so called source effects. Extending this study to coastal observatories is a natural step that can be developed in a future study. However, reproducing observations with modelling in coastal regions is more complicated due to the presence of conductive sediments. From our initial studies, a finer bathymetry resolution will be necessary to model tippers in these regions

(more details on Appendix A). On this regard, the General Bathymetric Chart of the Oceans (GEBCO) released a new bathymetry grid in 2019 with 0.15 arc-second horizontal resolution. We plan to use this bathymetry data to perform a similar modelling study in coastal observatories in the future.

The results obtained from this study can be used as an initial guideline on the regions where part the ocean effects need to be accounted for. Based on the observatories used in this study, this effect needs to be accounted for in the Pacific (GUA, PPT and HON observatories), Indian (CKI and GAN) and in the northern and southern regions of Atlantic Ocean (SMA and TDC, respectively). However, they are negligible in the equatorial Atlantic Ocean (ASC and SHE). They are also negligible in regions outside of the -30° to $+30^\circ$ latitude range, where oceanic conductivity variations with varying depths are negligible. The possible relations between other oceanic physical processes and tippers is a promising topic that can be explored in future studies.

In the experimental part of this dissertation I analyzed seasonal variations of tipper components measured on a global distribution of INTERMAGNET observatories. I estimated monthly tippers using a robust approach and grouped their corresponding variabilities into the three Lloyd seasons of the year to properly account for seasonal influences. Responses were calculated in all INTERMAGNET observatories with good data quality in the -60° to 60° latitude range, located in different tectonic settings, geological contexts and varying distances from the oceans. In total, 53 observatories were used, representing a significant improvement in comparison with previous studies (e.g. ARAYA VARGAS and RITTER, 2016; TAKEDA, 1997) since I analyzed seasonal variations in many low latitude observatories and specially in the southern hemisphere.

Seasonal modulations of both T_x components only have significant implications for EM inversions in latitudes larger than 35° and for periods larger than 1200 seconds only. Furthermore, in this region amplitude differences due to seasonal variations between both T_x components measured during different seasons may be large to affect EM inversions.

The real part of T_y component present seasonal modulations in large periods and latitudes with similar polarization as in $\Re T_x$, but with smaller amplitudes. However, in comparison with T_x variations, which are mostly restricted to the northern hemisphere, seasonal variations of this component can exceed the threshold in low latitudes as well, from -35° to 35° . Since in these latitudes most observatories are located in islands or close to oceans (Fig. 1), it may be that low latitude $\Re T_y$ seasonal variations are influenced by the geomagnetic coast effect (e.g. PARKINSON and JONES, 1979; SAMROCK and KUVSHINOV, 2013), characterized by anomalous B_z/B_y ratio along coastlines. For $\Im T_x$, modulations of D and J seasonal

variations were identified in all latitudes at 2400 s, but have negligible effects for EM inversions.

For all components, variations are negligible in the -60° to -35° latitude range. However, only 5 observatories are located in this region, which restricts further interpretations and raises the need to install more magnetic observatories in the southern hemisphere. Furthermore, amplitude of tipper variations measured during the equinox are smaller than for other seasons and in general have negligible effects for EM inversions. Thus, measuring tippers during this season can be useful to minimize seasonal variations in the aforementioned regions where they may be relevant, specially in the northern hemisphere.

The results from both steps of this dissertation highlight the necessity to properly account for anomalous effects when modelling and inverting tippers. They can also be used for an initial estimate of the regions where anomalous effects, either arising from the ocean or external magnetic fields, may affect responses. However, due to the complexity of the effects analyzed in this dissertation, the most appropriate way to account for them is to perform a regional analysis of the corresponding parameters, such as oceanic conductivity, and, if necessary, incorporate them into models.

Bibliography

- AMANTE, C., EAKINS, B. W., 2009, “ETOPO1 1 Arc-Minute Global Relief Model: Procedures, Data Sources and Analysis. NOAA Technical Memorandum NESDIS NGDC-24. National Geophysical Data Center, NOAA.” *doi:10.7289/V5C8276M*.
- ARAYA VARGAS, J., RITTER, O., 2016, “Source effects in mid-latitude geomagnetic transfer functions”, *Geophysics Journal International*, v. 204,1, pp. 606–630.
- ASTER, R., BORCHERS, B., THURBER, C., 2005, *Parameter estimation and inverse problems*. Waltham(MA), Elsevier Academic.
- AVDEEV, D. B., 2005, “Three-dimensional electromagnetic modelling and inversion from theory to application”, *Surveys in Geophysics*, v. 26, pp. 767–799.
- BANKS, R. J., 1969, “Geomagnetic Variations and the Electrical Conductivity of the Upper Mantle”, *Geophysics Journal International*, v. 17, n. 5, pp. 457–487.
- BEAMISH, D., 1979, “Source fields effects on transfer functions at mid-latitude”, *Geophys. J. R. astr. Soc.*, v. 58, pp. 117–134.
- BEAMISH, D., 1980, “Diurnal characteristics of transfer functions at pulsation period”, *Geophys. J. R. astr. Soc.*, v. 61, pp. 623–643.
- BEDROSIAN, P. A., FEUCHT, D. W., 2014, “Structure and tectonics of the northwestern United States from EarthScope USArray magnetotelluric data”, *Earth Planet. Sci. Lett.*, v. 402, pp. 275–289.
- BERDICHEVSKY, M. N., DMITRIEV, V., 2008, *Models and methods of magnetotellurics*. Springer, Berlin.
- BESIERIS, I. M., COMPTON, R., 1967, “Time-dependent Green’s function for electromagnetic waves in conducting media”, *Journal of Mathematical Physics*, v. 8, n. 12, pp. 2445–2451.

- BRÄNDLEIN, D., LÜHR, H., RITTER, O., 2012, “Direct penetration of the interplanetary electric field to low geomagnetic latitudes and its effect on magnetotelluric sounding”, *Journal of Geophysical Research*, v. 117, pp. 1–13.
- CABANES, C., GROUAZEL, A., VON SCHUCKMANN, K., et al., 2013, “The CORA dataset: Validation and diagnostics of in-situ ocean temperature and salinity measurements.” *Ocean Science*, v. 9, n. 1, pp. 1–18.
- CHAVE, A. D., JONES, A. G., 2012, *The magnetotelluric method: Theory and practice*. Cambridge University Press.
- CONSTABLE, S., 2015, *Geomagnetic induction studies*. In: *Treatise on Geophysics, 2nd edition*, v. 5. Elsevier.
- DOSSO, H., CHEN, J., 2000, “Analogue model study of EM induction in elongated conductors - 2D and 3D induction arrow responses.” *Earth, Planets and Space*, v. 52, n. 5, pp. 355–360.
- EGBERT, G., KELBERT, A., 2012, “Computational recipes for electromagnetic inverse problems”, *Geophysical Journal International*, v. 189, n. 1, pp. 251–267.
- FARQUHARSON, C. G., MIENSOPUST, M. P., 2011, “Three-dimensional finite-element modelling of magnetotelluric data with a divergence correction”, *J. Appl. Geophys.*, v. 75, pp. 699–710.
- FEISTEL, R., 2008, “A Gibbs function for seawater thermodynamics for -6 to 80° C and salinity up to 120 g kg⁻¹.” *Deep Sea Res. I.*, v. 55, pp. 1639–1971.
- GEBCO, 2019, “GEBCO Compilation Group (2019) GEBCO 2019 Grid”, [doi:10.5285/836f016a-33be-6ddc-e053-6c86abc0788e](https://doi.org/10.5285/836f016a-33be-6ddc-e053-6c86abc0788e).
- GIROD, B., RABENSTEIN, R., STENGER, A., 2001, *Signal and systems*. Wiley.
- GRAYVER, A. V., KOLEV, T. V., 2015, “Large-scale 3D geoelectromagnetic modeling using parallel adaptive high-order finite element method”, *Geophysics*, v. 80, n. 6, pp. 277–291.
- GRAYVER, A. V., MUNCH, F. D., KUVSHINOV, A. V., et al., 2017, “Joint inversion of satellite-detected tidal and magnetospheric signals constrains electrical conductivity and water content of the upper mantle and transition zone”, *Geophysical Research Letters*, v. 44, n. 12, pp. 6074–6081.

- GRAYVER, A. V., VAN DRIEL, M., KUVSHINOV, A. V., 2019, “Three-dimensional magnetotelluric modelling in spherical Earth.” *Geophysics. J. Int.*, v. 217, pp. 532–557.
- GREENBAUM, A., 1997, *Iterative methods for solving linear systems*. Philadelphia, USA.
- GREGORI, G. P., LANZEROTTI, L. J., 1980, “Geomagnetic depth sounding by induction arrow representation: A review”, *Reviews of geophysics and space physics*, v. 18, n. 1, pp. 203–209.
- GUZAVINA, M., GRAYVER, A. V., KUVSHINOV, A. V., 2019, “Probing upper mantle electrical conductivity with daily magnetic variations using global-to-local transfer functions.” *Geophysics. J. Int.*, v. 219, pp. 2125–2147.
- HERMANCE, J. F., 1978, “Electromagnetic induction in the Earth by moving ionospheric current systems.” *Geophys. J. R. astr. Soc.*, v. 55, pp. 557–576.
- HUBER, P., 1981, *Robust Statistics*. Wiley, New York.
- IOC, S. . A., 2010, “The international thermodynamic equation of seawater-2010: Calculation and use of thermodynamic properties, Intergovernmental Oceanographic Commission”, *Manual and Guides*, v. 56.
- JONES, A. G., SPRATT, J., 2002, “A simple method for deriving the uniform field MT responses in auroral zones.” *Earth, Planets and Space*, v. 54, pp. 443–450.
- KRUGLYAKOV, M., KUVSHINOV, A., 2018, “Using high-order polynomial basis in 3-D EM forward modeling based on volume integral equation method”, *Geophysics Journal International*, v. 213, pp. 1387–1401.
- KRUGLYAKOV, M., GERASKIN, A., KUVSHINOV, A., 2016, “Novel accurate and scalable 3-D MT forward solver based on a contracting integral equation method”, *Computers and Geosciences*, v. 96, pp. 208–217.
- KUVSHINOV, A. V., 2012, “Deep Electromagnetic Studies from Land, Sea and Space: Progress Status in the Past 10 Years”, *Survey Geophysics*, v. 33, pp. 169–209.
- KUVSHINOV, A. V., UTADA, H., AVDEEV, D., et al., 2005, “3-D modelling and analysis of Dst C-responses in the North Pacific Ocean region, revisited.” *Geophys. J. Int.*, v. 160, n. 2, pp. 502–526.

- KUVSHINOV, A. V., MANOJ, C., OLSEN, N., et al., 2007, “On induction effects of geomagnetic daily variations from equatorial electrojet and solar quiet sources at low and middle latitudes”, *Journal of Geophysical Research*, v. 112, n. B10102, pp. 1–13.
- MARCUELLO, A., QUERALT, P., LEDO, J., 2005, “Applications of dispersion relations to the geomagnetic transfer function”, *Physics of the Earth and Planetary Interiors*, v. 150, pp. 85–91.
- MARESCHAL, M., 1986, “Modelling of natural sources of magnetospheric origin in the interpretation of regional induction studies: A review.” *Survey in geophysics.*, v. 8, pp. 261–300.
- MORSCHHAUSER, A., GRAYVER, A. V., KUVSHINOV, A. V., et al., 2019, “Tippers at island geomagnetic observatories constrain electrical conductivity of oceanic lithosphere and upper mantle”, *Earth, Planets and Space*, v. 71, n. 1, pp. 17.
- MUNCH, F. D., GRAYVER, A. V., KUVSHINOV, A., et al., 2018, “Stochastic Inversion of Geomagnetic Observatory Data Including Rigorous Treatment of the Ocean Induction Effects With Implications for Transition Zone Water Content and Thermal Structure”, *Journal of Geophysical Research*, v. 123, pp. 31–51.
- MURPHY, B., EGBERT, G., 2018, “Source biases in midlatitude magnetotelluric transfer functions due to Pc3-4 geomagnetic pulsations”, *Earth, Planets and Space*, v. 70, n. 1, pp. 12.
- NABIGHIAN, M. N., 1991a, *Electromagnetic methods in applied geophysics - Part A*, v. 2. Society of Exploration Geophysics.
- NABIGHIAN, M. N., 1991b, *Electromagnetic methods in applied geophysics - Part B*, v. 2. Society of Exploration Geophysics.
- OLSEN, N., 1998, “The electrical conductivity of the mantle beneath Europe derived from C-responses from 3 to 720 hr.” *Geophysics. J. Int.*, v. 133, n. 2, pp. 298–308.
- ORDINANCE, 2016, *A guide to coordinates systems in Great Britain. An introduction to mapping coordinate systems and the use of GNSS datasets with Ordinance Survey mapping; Version 3.0.*

- PANKRATOV, O., KUVSHINOV, A., 2015, “Applied mathematics in EM studies with special emphasis on an uncertainty quantification and 3-D Integral Equation modelling”, *Geophys. J. R. Ast. Soc.*, v. 37, n. 1.
- PANKRATOV, O., AVDEEV, D., KUVSHINOV, A., 1995, “Electromagnetic field scattering in a heterogeneous Earth: A solution to the forward problem”, *Izvestiya, Physics of the Solid Earth*, v. 31, n. 3, pp. 201–209.
- PARKINSON, W., 1959, “Directions of rapid geomagnetic fluctuations.” *Geophys. J. R. Ast. Soc.*, v. 2, pp. 1–14.
- PARKINSON, W., JONES, F. W., 1979, “The geomagnetic coast effect”, *Reviews of Geophysics and Space Physics*, v. 17, n. 8, pp. 1999–2017.
- PETEREIT, J., SAYNISCHE-WAGNER, J., IRRGANG, C., et al., 2019, “Analysis of ocean-tide induced magnetic fields derived from oceanic in situ observations: Climate trends and the remarkable sensitivity of shelf regions.” *Journal of Geophysical Research: Oceans*, v. 124, pp. 8257–8270.
- PÜTHE, C., 2015, “Interpretation of global EM induction data from ground, sea and space: new response functions, inversion schemes and conductivity models”, *ETH Zürich Research Collection, Doctoral Thesis*.
- PÜTHE, C., KUVSHINOV, A., OLSEN, N., 2015, “Handling complex source structures in global EM induction studies: from C-responses to new arrays of transfer functions”, *Geophysical Journal International*, v. 201, pp. 318–328.
- RAO, C. K., JONES, A. G., MOORKAMP, M., et al., 2014, “Implications for the lithospheric geometry of the Iapetus suture beneath Ireland based on electrical resistivity models from deep-probing magnetotellurics”, *Geophys. J. Int.*, v. 198, pp. 737–759.
- SAMROCK, F., KUVSHINOV, A., 2013, “Tipper at island observatories: Can we use them to probe electrical conductivity of the Earth’s crust and upper mantle?” *Geophysical Research Letters*, v. 40, pp. 824–828.
- SAMROCK, F., KUVSHINOV, A., BAKKER, J., et al., 2015, “3-D analysis and interpretation of magnetotelluric data from the Aluto-Lugano geothermal field, Ethiopia”, *Geophysical Journal International*, v. 202, pp. 1923–1948.
- SCHMUCKER, U., 1999, “A spherical harmonic analysis of solar daily variations in the years 1964-1965: Response estimated and source fields for global induction- II. Results”, *Geophysics J. Int.*, v. 6, pp. 441–449.

- SEMENOV, A., 2011, “Global 3-D imaging of mantle electrical conductivity based on inversion of observatory C-responses: an approach, data analysis and results”, *ETH Zürich Research Collection*, v. Doctoral Thesis.
- SEMENOV, A., KUVSHINOV, A., 2012, “Global 3-D imaging of mantle conductivity based on inversion of observatory C-responses - I. An approach and its verification”, *Geophysical Journal International*, v. 189, n. 3, pp. 1335–1352.
- SHIMIZU, H., KOYAMA, T., BABA, K., et al., 2010, “Revised 1-D mantle electrical conductivity structure beneath the North Pacific.” *Geophysical Journal International*, v. 180, pp. 1030–1048.
- SIMPSON, F., BAHR, K., 2005, *Practical Magnetotellurics*. Cambridge(UK), Cambridge University Press.
- SOKOLOVA, E. Y., VARENTSOV, T., 2007, “Deep array electromagnetic sounding on the Baltic Shield: External Excitation model and implications for upper mantle conductivity studies.” *Tectonophysics*, v. 445, pp. 3–25.
- STRAUME, E. O., GAINA, C., MEDVEDEV, S., et al., 2019, “GlobSed: Updated total sediments thickness in the world’s oceans”, *Geochemistry, Geophysics, Geosystems*, v. 20, pp. <https://doi.org/10.1029/2018GC008115>.
- TAKEDA, M., 1997, “Local time variation of geomagnetic transfer functions”, *Geophys. J. Int.*, v. 130, n. 3, pp. 765–770.
- TIETZE, K., RITTER, O., 2013, “Three-dimensional magnetotelluric inversion in practice?the electrical conductivity structure of the San Andreas Fault in central California.” *Geophys. J. Int.*, v. 195, pp. 130?147.
- TYLER, R. H., BOYER, T. P., MINAMI, T., et al., 2017, “Electrical conductivity of the global ocean”, *Earth, Planets and Space*, v. 69, pp. 156.
- UTADA, H., KOYAMA, T., SHIMIZU, H., et al., 2003, “A semi-global reference model for electrical conductivity in the mid-mantle beneath the North Pacific region”, *Geophysical Research Letters*, v. 30, n. 4, pp. 1194.
- VILJANEN, A., PIRJOLA, R., AMM, O., 1999, “Magnetotelluric source effect due to 3D ionospheric current systems using the complex image method for 1D conductivity structures.” *Earth, Planets, Space.*, v. 51, pp. 933–945.
- YAMAZAKI, Y., MAUTE, A., 2017, “Sq and EEJ - A review on the daily variation of the geomagnetic field caused by ionospheric dynamo currents”, *Space Science Reviews*, v. 206, pp. 299–405.

YANG, B., EGBERT, G. D., KELBERT, A., et al., 2015, “Three-dimensional electrical resistivity of the north-central USA from EarthScope long period magnetotelluric data.” *Earth Planet Sci. Lett.*, v. 422, pp. 87–93.

YOSHINO, T., 2010, “Laboratory-based electrical conductivity in the Earth’s mantle”, *Surveys in Geophysics*, v. 31, n. 2, pp. 163–206.

Appendix A: Modelling of Tippers in Coastal Regions

Modelling results for two coastal observatories, King Edward Point (KEP; $\theta = -54.28^\circ, \phi = -36.49^\circ$), Kourou (KOU; $\theta = -5.21^\circ, \phi = -52.73^\circ$) and Port Stanley (PAF; $\theta = -51.7^\circ, \phi = -57.89^\circ$), are presented in Figures A3 and A4, respectively. Bathymetry (Figures A3 a and A4 a) are approximately constant in the y direction, as can be observed in Figures A3 (b) and A4 (b) (compare those with the bathymetry profiles presented in Chapter 5). It can be seen that modelled tipper components curves, presented on Figures A3 (d) to (g) and A4 (d) to (g), deviates significantly from observations in all periods from 300 s to 10000 s.

A possible explanation for this misfit is the presence of conductive sediments in coastlines. Sediment thickness data from GlobSed model (STRAUME *et al.*, 2019) are presented on Figure A1. It can be seen that sediment thickness is expressive in all coastlines worldwide, except in the western american coast. Coastal sediments can accumulate in vertical layers with up to 18 km thickness, thus it is necessary to incorporate this feature in models. Moreover, sediment thickness is negligible in the island observatories modelled in this study.

Moreover, from our initial tests it may be necessary to use a finer bathymetry data resolution to resolve for small scale conductive structures in coastal regions. This issue is illustrated on the discretized conductivity model created for Tatuoca observatory (TTB; $\theta = 1.2^\circ, \phi = -48.5^\circ$), presented in (Figure A2 a). Comparing the created model with the map of the island (Figure A2 b), it can be observed that the current resolution of bathymetry data is not fine enough to reproduce the complexity of conductive structures in this region. The General Bathymetric Chart of the Oceans (GEBCO) released a new bathymetry grid in 2019 with 0.15 arc-second horizontal resolution that can be used to improve modelling in this situation. However, incorporation of this new bathymetry and sediment thickness datasets, and all the tests associated to incorporate these features, is beyond the scope of this study.

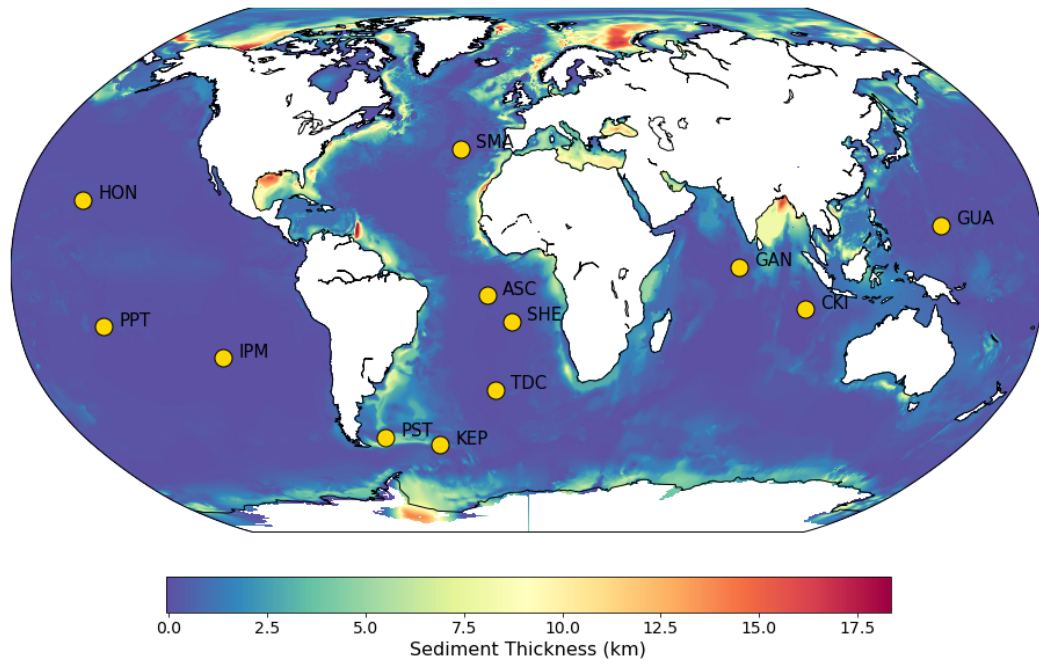


Figure A1: Global sedimentary thickness map. Data is from GlobSed model (STRAUME *et al.*, 2019). Yellow circles represent observatories used in modelling.

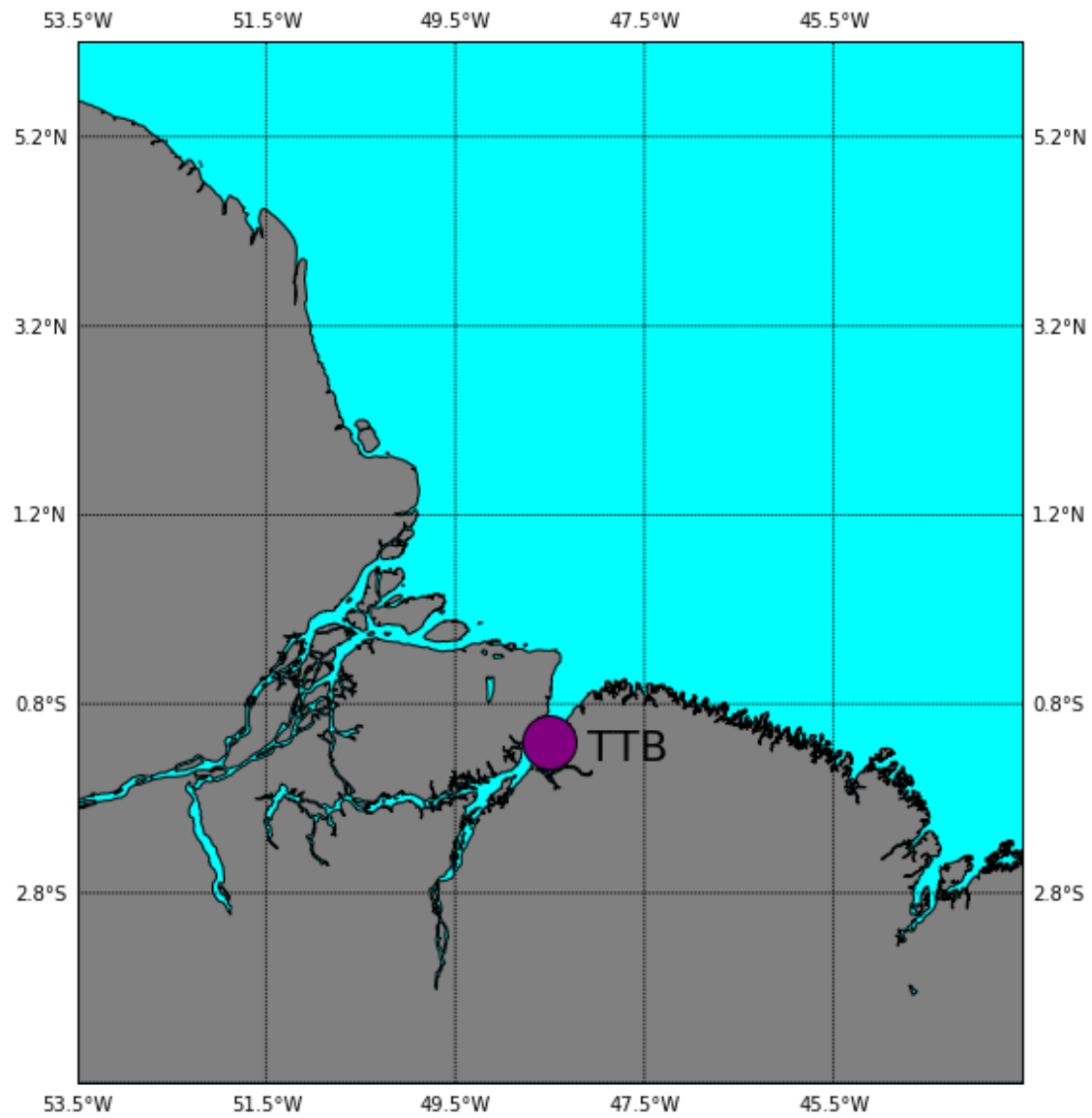


Figure A2: Tatuoca observatory (TTB; $\theta = 1.2^\circ$, $\phi = -48.5^\circ$) discretized conductivity model (a) and map (b).

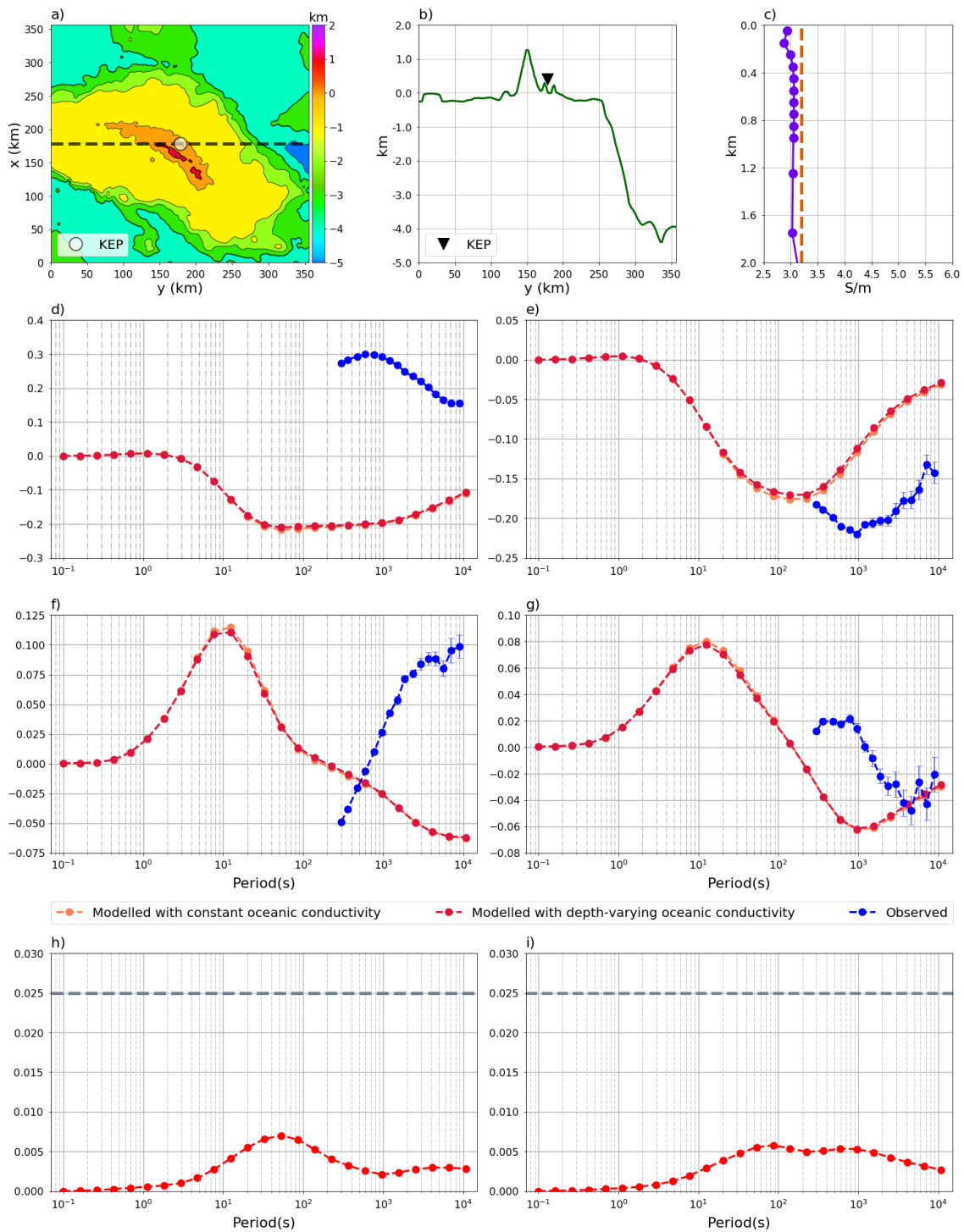


Figure A3: Same as Figure ??, but for King Edward Point observatory (KEP; $\theta = -54.28^\circ$, $\phi = -36.49^\circ$).

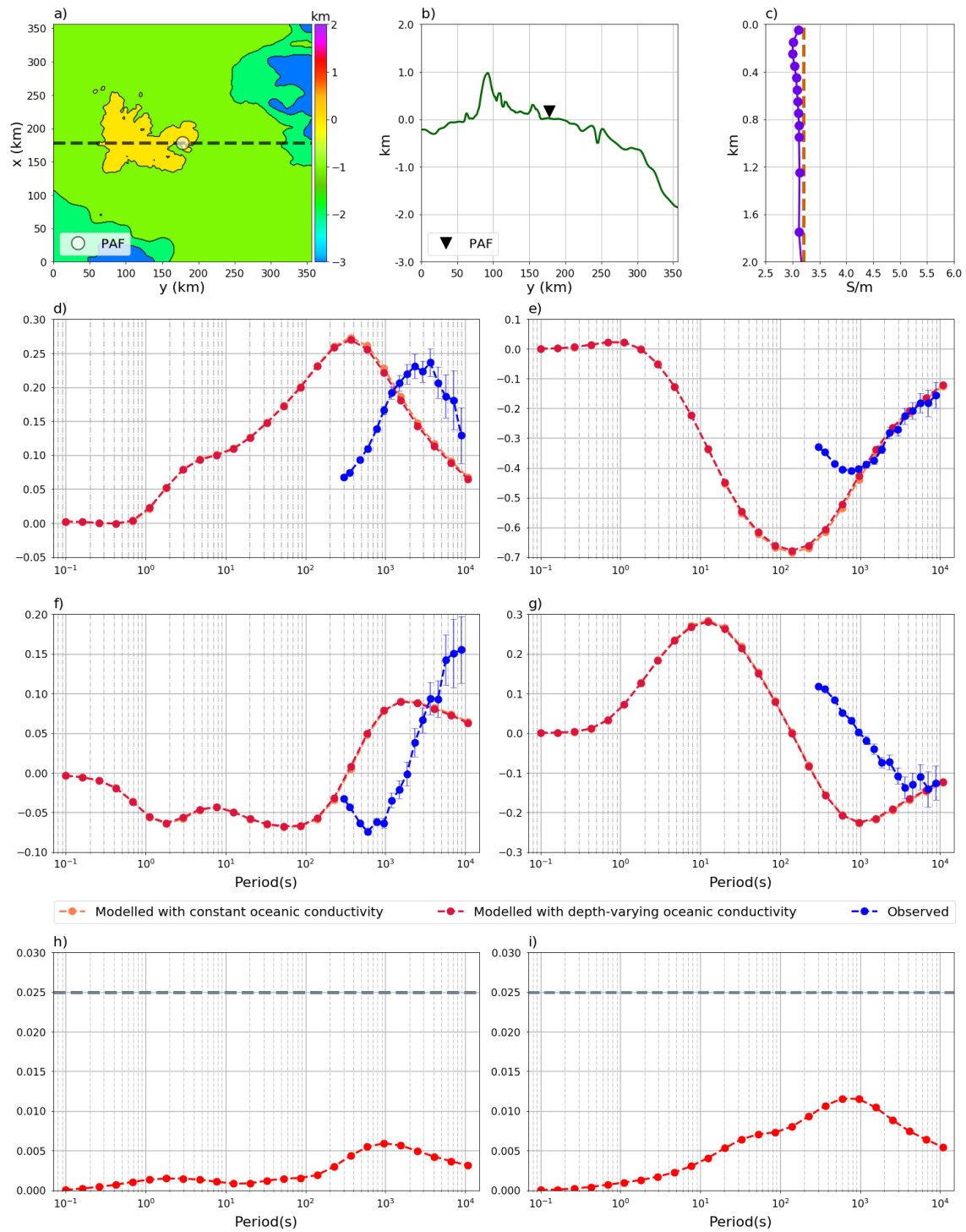


Figure A4: Same as Figure ??, but for Port Stanley observatory (PAF; $\theta = -51.7^\circ$, $\phi = -57.89^\circ$),

Appendix B: Abstract submitted to Earth, Planets, Space (EPS) journal

The experimental data part of this dissertation was submitted as an express letter to the Earth, Planets, Space (EPS) journal at the 25th of January, 2020. The title of this paper is "Investigating seasonal modulations of tippers measured in a global distribution of magnetic observatories". Rafael Rigaud is the main author of this paper and Katia Pinheiro is the co-author. The abstract of this paper is presented as follows.

"Vertical magnetic transfer functions (tippers) can be calculated from magnetic observatory data to investigate electrical conductivity variations up to 200 km depth. The application of this technique relies on the approximation of external magnetic source fields as homogenous plane waves in the region of measurements. Deviations from the plane wave assumption can result in biased responses due to anomalous source fields, such as seasonal modulations of the northward tipper components observed in mid-latitude observatories. We extend this analysis to a worldwide distribution of INTERMAGNET observatories. We calculate monthly tippers and variabilities using a robust section-averaging approach and group their corresponding variabilities into the Lloyd seasons of the year. We show that, for the northward tipper components, seasonal variations have implications for electromagnetic (EM) inversion only in latitudes larger than 35° and for periods larger than 1200 seconds. Moreover, in these regions there are large amplitude differences between northward tipper components measured in December and June solstices that need to be accounted for when comparing responses measured during different seasons. For the real eastward tipper component, seasonal variations can be relevant for EM inversions in a larger latitude range, from -35° to 60° , and for periods larger than 2400 seconds. For the imaginary eastward component, seasonal modulations are observed in all latitudes at 2400 seconds, but they are negligible for EM studies. For both components, variations of tippers measured during the equinox are negligible. Thus, measuring data during this season can be effective to minimize seasonal source effects in the aforementioned regions."

Appendix C: Abstract to be submitted to Earth, Planets, Space (EPS) journal

The modelling part of this dissertation will be submitted as a full paper to the Earth, Planets, Space (EPS) journal. The planned date of submission is April, 2020. The title of this paper is "Exploring Variability of Tippers at Island Magnetic Observatories due to Realistic Variations of Oceanic Electrical Conductivity". Rafael Rigaud is the main author and Mikhail Kruglyakov, Alexey Kuvshinov, Katia Pinheiro, Elena Ivannikova and Johannes Petereit are the co-authors. The abstract of this paper is presented as follows.

"Magnetic observatories around the world continuously measure time variations of the three components of the geomagnetic field. Long-period (> 3 hours) variations are traditionally used to constrain electrical conductivity of the Earth's mantle either in terms of one-dimensional (1-D) or three-dimensional (3-D) conductivity distributions. Recent studies have also shown that tippers estimated from short-period (< 3 hours) variations at island observatories can constrain 1-D conductivity distributions of the oceanic lithosphere and upper mantle. This becomes feasible due to the ocean induction effect (OIE) which originates from lateral conductivity contrasts between ocean and land., and which leads to non-zero tippers even in the situation when the conductivity distribution beneath an observatory is 1-D. Proper analysis of island tippers requires an accurate 3-D modeling of OIE. So far such a modeling is performed in an assumption that the oceanic conductivity is constant through the depth, in spite of the fact that oceanic conductivity varies significantly within the first few hundred meters of water column. In this study we explore – using rigorous 3-D electromagnetic (EM) modeling – at what extent realistic depth-varying oceanic conductivity affects island tippers. The modeling is performed for 10 island observatories around the world, and in the period range ($10^{-1} - 10^4$ sec) where OIE in tippers is expected to be perceptible. Furthermore, we address the problem of temporal variability of the tippers. It is known that tippers reveal systematic seasonal variability whose origin is believed to be associated with external magnetic source

fields. We explore, again, using 3-D EM modeling, whether part of this variability is due to temporal changes of oceanic conductivity. Our model studies suggest that in most of considered island observatories the effect from depth-varying oceanic conductivity is tangible, exceeding the error floor (0.025) which is usually assigned to tippers during their inversion. Contrary, the effects from time-varying oceanic conductivity appeared to be too small to be worth consideration."